Theme: Air/Water Quality

Case Study 1

Remote-Sensing Case Study of the Chesapeake Bay Region during Drought (2002) and Flood (2003) Years

James Acker*[1] **and Zhong Liu**[2]

1.1 Background Information

The location of this study is the Chesapeake Bay estuary on the eastern Mid-Atlantic coast of the United States. The Chesapeake Bay system is the largest estuary in the United States and one of the largest in the world. Chesapeake Bay is approximately 320 kilometers long, with its mouth located in Virginia near Norfolk and Hampton Roads, to the upper part of the Bay at Havre de Grace, Maryland. The headwaters of the Susquehanna River (one of the major rivers entering the bay) are located near Cooperstown, New York. The Chesapeake Bay watershed is approximately 166,000 square kilometers, and the Bay itself has over 18,000 km of shoreline. The average depth of the Chesapeake Bay is about 6.5 meters, though it can be deeper than 45 meters in some locations.

Fresh water from five major rivers enters the Bay - these rivers are the Susquehanna, Potomac, James, York, and Rappahannock. Although there are many other rivers and streams feeding into the bay, about 90% of the fresh water input to the bay comes from these five rivers. Due to the large amount of fresh water delivered by the Susquehanna River, the upper portion of the Bay has much lower salinity than the lower portion of the Bay, where tidal flow from the Atlantic is significant. It is estimated that a roughly equal volume of salt water enters the Bay from the Atlantic compared to the volume of fresh water entering the Bay from river systems.

Due to the size of the estuary and the volume of fresh water that enters it, the physical characteristics of Chesapeake Bay water and the biological dynamics of the bay are strongly connected the flow of water and the quality of the water entering it from land. A large percentage of the bay's watershed land is used for agriculture, particularly in Pennsylvania and the Eastern Shore of Maryland. This land usage

---

[1] Goddard Earth Sciences Data and Information Services Center, Wyle IS LLC, NASA GES DISC Code 610.2, Greenbelt, MD 20771, USA. **Email address:* `james.g.acker@nasa.gov`

[2] Goddard Earth Sciences Data and Information Services Center, George Mason University, USA

results in large amounts of nutrients derived from agricultural fertilizer and animal wastes entering the bay in runoff from fields. A further influence on the bay waters is the increasing population and urban development in major cities, which include Washington D.C., Baltimore (Maryland), Richmond (Virginia) and Scranton/Wilkes-Barre (Pennsylvania), and many other smaller cities and towns in the watershed. Developmental sprawl means that an increasing area of the watershed is impervious to water penetration, resulting in increased runoff and additional input of nutrients and pollutants, as well as input from the growing human population. Therefore, the general quality of bay waters and the ability to host marine flora and fauna, which is subject to increasing environmental stress, is directly connected to the hydrological system of the Chesapeake Bay watershed.

During the year 2002, much of the United States experienced severe to extreme drought conditions. These conditions were acute in two locations: most states west of the Dakotas, Nebraska, Kansas, Oklahoma, and Texas; and the eastern seaboard from southern Georgia to New Jersey. On the eastern seaboard, the central portion of North and South Carolina, Virginia, and Maryland were subject to particularly acute conditions; the situation worsened in Virginia and Maryland during summer and autumn 2002, with some communities in these states imposing severe water use restrictions, and reservoirs dropping to very low capacities. One reservoir serving Baltimore dropped to 16% capacity and was estimated to have only a 30-day supply of water remaining.

Rain in late autumn began to alleviate the drought conditions, and the rain pattern persisted and became much stronger in the spring of 2003. Rainfall in March and April was particularly heavy in Virginia and Maryland. Over the course of the entire year of 2003, the Baltimore region set an annual precipitation record – a very distinct contrast from the dry conditions that had characterized much of 2002.

Due to these significantly different hydrological conditions, it was expected that the waters of the Chesapeake Bay would exhibit distinctly different bio-optical characteristics, related to the volumes of fresh water and associated nutrient transport during low- and high-flow conditions. The availability of ocean-colour radiometry data in the online data analysis system created by the NASA Goddard Earth Sciences Data and Information Services Center (GES DISC) provided the opportunity to investigate the effects of the "drought and flood" precipitation pattern on the waters of the Chesapeake Bay, which is the subject of this case study (Acker et al. 2005).

Three remotely-sensed variables, chlorophyll-*a* concentration (chl-*a*), the diffuse attenuation coefficient at 490 nm (K490), and remote-sensing reflectance at 555 nm (R_{rs}555) will be used to examine the bio-optical characteristics of the Chesapeake Bay waters. Chl-*a* reflects the concentration of phytoplankton, the floating photosynthetic plants that form the base of the marine food chain. Phytoplankton are primary producers, creating carbon biomass through the process of photosynthesis. The photosynthetic pigment chlorophyll contained in their cells enables this process, and thus chl-*a* is an indicator of the prevalence of phytoplankton. Since, in addition to sunlight, phytoplankton require dissolved nutrients (primarily nitrate and phosphate) in seawater to grow, phytoplankton populations will grow more rapidly and abundantly in the presence of elevated nutrient concentrations. When this happens, an overabundance of phytoplankton can cause increased deposition of dead phytoplankton organic material on the estuarine bottom or seafloor. The digestion ("respiration") of this organic matter by bacteria uses dissolved oxygen in the water, which is important for most organisms living in the water. Increased bacterial respiration of organic matter can reduce dissolved oxygen so much that the water cannot support aquatic life.

Remote sensing estimates the concentration of chl-*a* by detecting the absorption of light by the chlorophyll in phytoplankton cells. It should also be noted that in turbid waters, remotely-sensed chl-*a* can be overestimated due to the absorption or reflection of light by other substances. This is an important point in many areas, but will be less important here.

K490 is simply a measure of how much the intensity of light entering the oceanic water column is attenuated (reduced) by interaction with substances either dissolved or suspended in the water, either through light absorption, light scattering, or light reflection. High values of K490 thus indicate more turbidity, and low values of K490 indicate less turbidity. Turbidity can be caused by increased concentrations of phytoplankton, suspended sediments, or dissolved substances, and usually is a combination of all three of these factors.

$R_{rs}555$ indicates light reflection, as there is very little absorption of light at this wavelength in marine waters. Thus, $R_{rs}555$ is sensitive to the presence of suspended sediments, which reflect and scatter light without absorbing much light. Light at a wavelength of 555 nm will also be reflected off the seafloor when the water depth is sufficiently shallow for the light to penetrate to the bottom and reflect back toward the surface.

1.2 Materials and Methods

The primary data set for this investigation is ocean-colour radiometry (OCR) data acquired by the Sea-viewing Wide Field-of-view Sensor (SeaWiFS). SeaWiFS has been in nearly continuous operation since September 1997 and provides an exemplary calibrated remotely-sensed data set of ocean-colour variables, including chlorophyll-*a* concentration (chl-*a*) and the diffuse attenuation coefficient at 490 nm (K490).

The algorithm for the chl-*a* retrieval, OC4V4, is an empirical algorithm based on ratios of reflectances for the SeaWiFS bands at 443, 490, 510, and 555 nm (O'Reilly et al., 2000). The K490 algorithm uses data from the SeaWiFS band at 490 nm (Mueller and Trees, 1997).

SeaWiFS ocean-colour data will be analyzed utilizing the GES DISC Interactive Online Visualization ANd aNalysis Infrastructure (Giovanni) (Acker and Leptoukh, 2007). Giovanni will be used to generate maps of data products over the Chesapeake Bay during the spring months of 2002 and 2003, to contrast the low-flow conditions of 2002 with the high-flow conditions of 2003. The three data products that will be examined are chl-*a*, K490 and $R_{rs}555$. To use Giovanni, a region of interest is selected either by clicking-and-dragging the display cursor on an interactive map, or by providing latitude-longitude corner points defining a specific region of interest. For this study, the corner points are provided to ensure uniformity of output visualizations. The time period of interest is specified for the spring months of 2002 and 2003.

Additional images are provided for context of the Chesapeake Bay region. URLs for these images are provided below. The MODIS images show the Chesapeake Bay, highlighting the major rivers and urban areas, and also demonstrating differences in land use patterns. The watershed image shows the regional extent of the Chesapeake Bay watershed. The impervious surface maps show that urbanization increases impervious surface area around the Chesapeake Bay (these are numbered Figures 1.6 to 1.8.)

Chesapeake Bay watershed:
`http://veimages.gsfc.nasa.gov/20832/image04162006_1km.jpg`
Impervious surface, State of Maryland:
`http://www.dnr.state.md.us/watersheds/surf/indic/md/md_pctimp_indmap.html`
Impervious surface, urban areas in the Chesapeake Bay watershed:
`http://www.whrc.org/midatlantic/mapping_land_cover/products/impervious_surfaces.htm`

1.3 Demonstration Section

The use of Giovanni provides the capability for users to generate their own images, rather than relying on previously-created images. Thus, the instructions in this demonstration section and the associated images will show how to create the images, and subsequently how to interpret them. There are no large image files that have to be opened; small images will be shown here to demonstrate what the end result should look like.

Step 1: Go to the Giovanni Ocean Color Radiometry Interface:
`http://gdata1.sci.gsfc.nasa.gov/daac-bin/G3/gui.cgi?instance_id=ocean_month`

Step 2: Enter the geographical coordinates below the interactive map. West: -77.5 North: 40.0 South: 36.5 East: -75.0. Click the "Update Map" button. This will show the highlighted region, with the Chesapeake Bay inside the box defined by the coordinates.

Step 3: In the SeaWiFS.R2009 data set (the first data set listed), select the following parameters by clicking in the boxes on the left next to the parameter name:

Chlorophyll-*a* concentration, Diffuse attenuation coefficient at 490 nm, Remote sensing reflectance at 555 nm.

Step 4: In the calendar selection menu below the lists of parameters, select the following time period: Begin Date: Year = 2002, Month = April, End Date: Year = 2002, Month = Jun (June).

Step 5: Click the "Generate Visualization" button. The default option, "Lat-Lon Map, Time-Averaged", is the visualization option that will be utilized here. The Giovanni system will now generate the visualizations for the three selected parameters. When the maps have been generated, click on the "Download Data" tab at the top. Go to the "Output Files" section, and click on each filename listed. This will display the visualization. Download the images into a folder according to the method for image download appropriate to the Web browser that is being used. It may be necessary to add the suffix ".gif" to the filename in order to see the images in the folder. When the image has been downloaded, click the "Back" button on the browser and repeat the process until all the images have been downloaded.

Step 6: Click the "Visualization Results" tab. Now use the calendar menu to change the dates to the following. All that is changed is the year, from 2002 to 2003. Begin Date: Year = 2003, Month = April, End Date: Year = 2003, Month = Jun (June). Go to the bottom of the page and click the "Submit Refinements" button. The Giovanni system will now create the visualizations for the same data parameters for this second time period. **The bio-optical and optical parameter visualizations have now been generated.**

Steps 7–11 below will generate the TRMM precipitation maps for two consecutive nine-month periods in the years 2002 and 2003.

Step 7: Go to the Daily TRMM and Other Rainfall Estimate interface:
`http://gdata1.sci.gsfc.nasa.gov/daac-bin/G3/gui.cgi?instance_id=TRMM_3B42_Daily`

Step 8: Enter the following geographic coordinates: West: -81.0, North: 43.0, South: 36.0, East: -73.0. Click the "Update Map" button. This will show the highlighted region.

Step 9: The only parameter available, "precipitation", should already be selected. Click the box if it is not selected.

Step 10: Enter the following temporal information: Begin Date: Year = 2002, Month = Jan (January), Day = 01, End Date: Year = 2002, Month = Sep (September), Day = 30. Then click the "Generate Visualization" button. The default option, "Lat-Lon Map, Time-Averaged", is the visualization option that will be utilized here. Next to this option, click the "Edit Preferences" button. Scroll down to the "Color Bar" section, and change the "Mode" choice from Pre-Defined to Custom. In the "Min Value" box, enter 0.0. In the "Max Value" box, enter 6.4. Now go to the bottom of the page and click the "Generate Visualization" button. The Giovanni system will now generate the visualization for the precipitation parameter. When the visualization is completed, save the image using the same procedure as in Step 5.

Step 11: Change the temporal information to the following: Begin Date: Year = 2002, Month = Oct (October), Day = 01, End Date: Year = 2003, Month = Jun (June), Day = 30. Go to the bottom of the page and click the "Submit Refinements" button. The Giovanni system will now create the map visualization of the precipitation parameter for this second time period. **The precipitation parameter visualizations have now been generated.**

1.3.1 Image Interpretation

Now that the visualizations have been generated, it is time to examine them for basic interpretation of these results. Each of these images depicts the data values utilizing a false-colour palette. The colour palette used in all cases here is the common "rainbow" palette, in which higher values of the data parameter are expressed in warmer colours (i.e. orange and red), low values are cooler colours (blue and purple), and intermediate values are greens and yellows. For chlorophyll-*a* data, the colour scale is logarithmic, so that the highest values are about 400-800 times greater than the lowest values. The scale for all of the other parameters is linear. Using the colour palette, interpretation of the images is straightforward. Each image shows a map of the values of the parameter averaged over the selected time period. These maps allow easy recognition of where the values were higher and lower in the region during the selected time period.

For the chl-*a* images, the highest values in the orange and red range show areas where phytoplankton chlorophyll concentration was elevated. This usually indicates where phytoplankton populations were thriving. Remotely-sensed chl-*a* can sometimes exhibit erroneously high values if there is a significant concentration of coloured dissolved organic matter (CDOM) also present in the water. Remember that the values of chl-*a*, and also K490 and $R_{rs}555$, were averaged over a three-month period. The concentrations on any given day during the month could have been much higher or lower than the average calculated over three months.

For the K490 images, higher values indicate where the water was more turbid, i.e., where incoming light was attenuated more strongly due to the presence of interfering substances or particles in the water. For the $R_{rs}555$ images, higher values indicate where incoming light at this wavelength was reflected more strongly back toward the satellite sensor.

The TRMM precipitation data maps are also easy to interpret using the ‘rainbow’ palette. The warmer colours (higher values) indicate higher amounts of precipitation

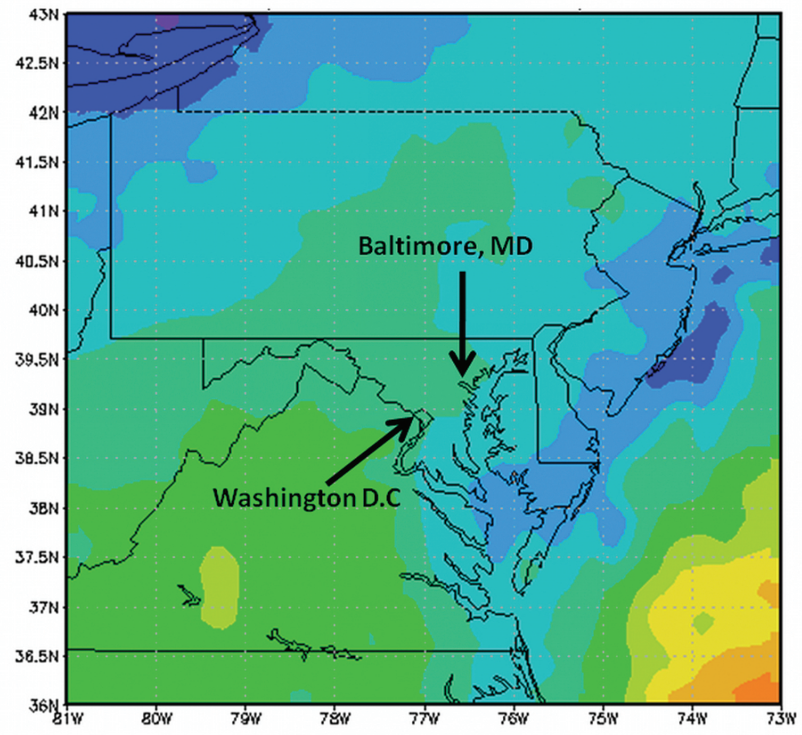

Figure 1.1 Location map of the Chesapeake Bay with TRMM precipitation data, showing location of Washington DC, and Baltimore, MD.

averaged over the nine-month time period. The average amount of precipitation indicates approximately the amount of rain that fell on a per-day basis in a given location over the entire time period. Of course, it is unlikely that there was rain on most of those days, so the average precipitation per day gives a general indication of the amount of rainfall the region received during the specified period of time. If the average value of mm/day is multiplied by the number of days in the period (about 270 for a nine-month period), this would give the approximate total amount of rainfall for that period. So an average precipitation amount of 3 mm/day means that about 800mm (or 30 inches) of rain fell during that period.

1.4 Training and Questions

Now we will examine each of the image pairs in turn to evaluate the environmental forcing in the Chesapeake Bay watershed and the effects that this forcing had on the bio-optical conditions in the Chesapeake Bay. The first set of images to examine is the pair of TRMM precipitation maps. Examine the labelled precipitation map (Figure 1.1 above) that shows the locations of Washington D.C. and Baltimore (note: this map used a different colour palette scale). Answer questions 1 and 2 below using Figure 1.2 depicting the average precipitation during the period 1 January to 30 September 2002.

Q 1: What was the average daily precipitation for the region including Washington D.C. and Baltimore?

Q 2: What was the approximate total precipitation for this region?

For the map depicting the average precipitation during the period of 1 October 2002 to 30 June 2003 (Figure 1.2b):

Q 3: What was the average daily precipitation for the region including Washington D.C. and Baltimore?

Q 4: What was the approximate total precipitation for this region? Now consider the potential implications of the different rainfall amounts for the region.

Q 5: What would be the effects of the markedly different rainfall amounts on the volume of water flowing in the streams and rivers in the Chesapeake Bay watershed?

Q 6: What differences would be expected on the amount of fresh water entering the Chesapeake Bay during the two periods that were depicted in the precipitation maps?

The next pair of images to examine is the pair of chl-*a* maps of the Chesapeake Bay. Examine the two maps side-by-side. Figure 1.3a depicts chl-*a* during April – June 2002, and Figure 1.3b depicts chl-*a* during April – June 2003.

Q 7: During which period are the chl-*a* values in the Bay significantly higher?

Q 8: Does this period of time correspond to the period when precipitation in the Chesapeake Bay watershed region was low (January – September 2002) or high (October 2002 – June 2003)?

Q 9: Given that higher chl-*a* values likely indicate higher values of phytoplankton productivity, what relationship may exist between precipitation, stream-flow, and phytoplankton productivity in the Chesapeake Bay? What could be the cause(s) of that relationship?

The next pair of images to examine is the pair of K490 maps of the Chesapeake Bay. Also examine the two maps side-by-side. Figure 1.4a depicts K490 during April – June 2002, and Figure 1.4b depicts K490 during April – June 2003.

Q 10: During which period are the K490 values in the Bay significantly higher?

Q 11: Does this period of time correspond to the period when precipitation in the Chesapeake Bay watershed region was low (January – September 2002) or high (October 2002 – June 2003)?

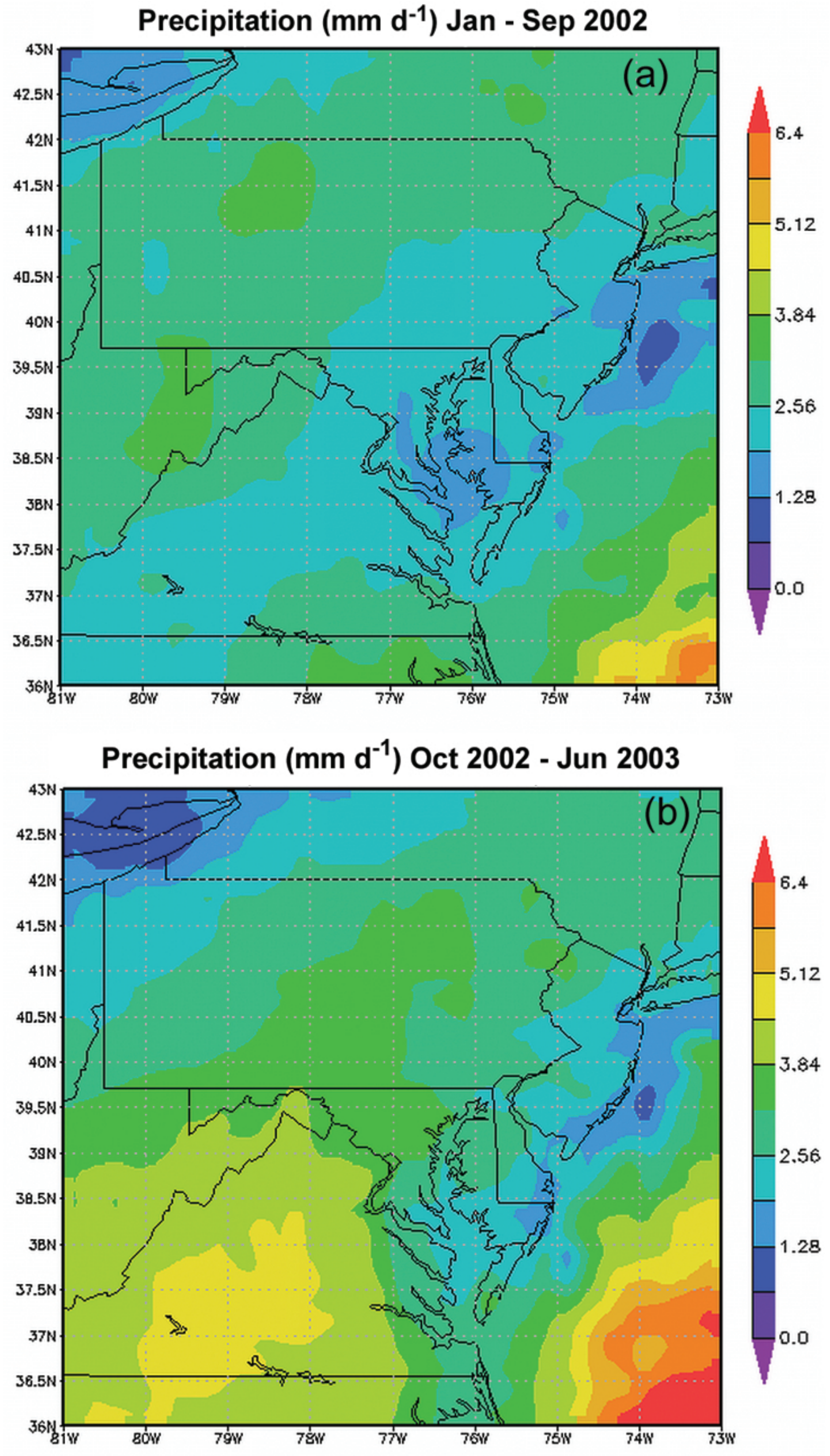

Figure 1.2 (a) Average daily precipitation over the Chesapeake Bay watershed region, January – September 2002, (b) Average daily precipitation over the Chesapeake Bay watershed region, October 2002 – June 2003.

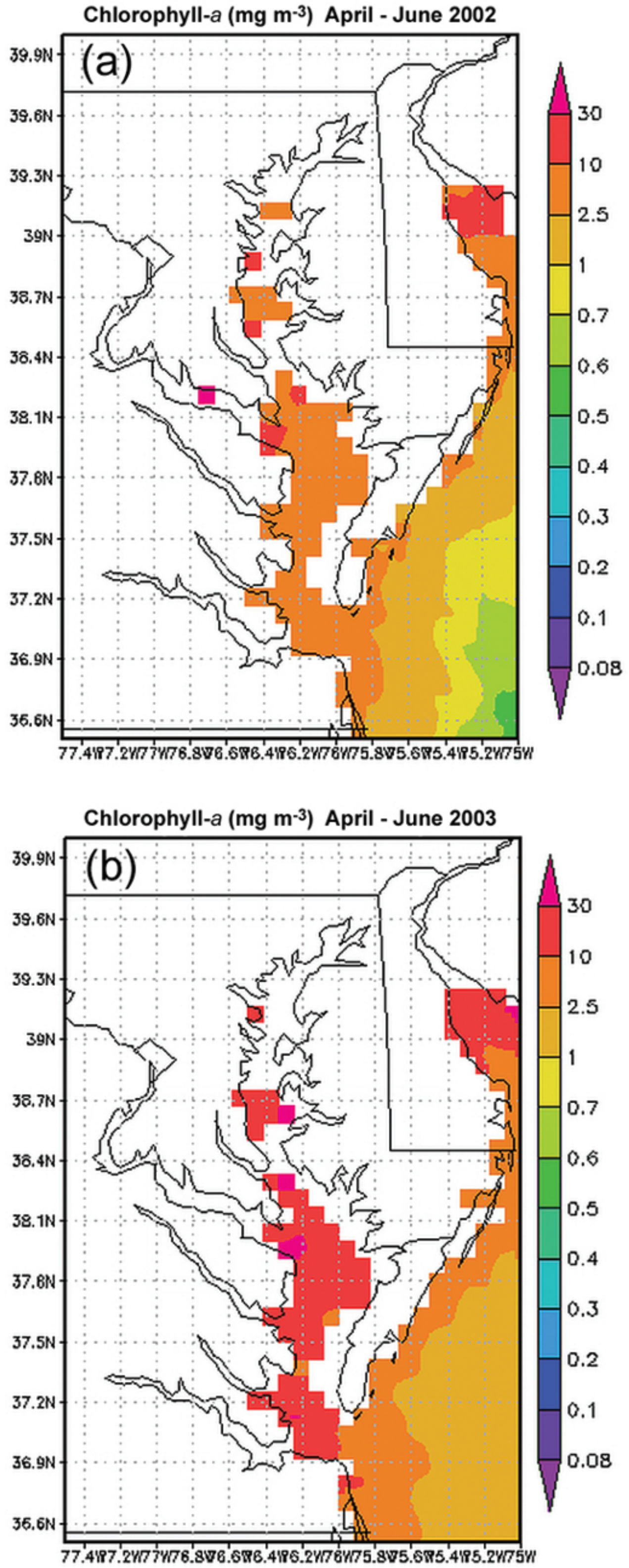

Figure 1.3 (a) Average chl-*a* in the Chesapeake Bay, April – June 2002 (b) Average chl-*a* in the Chesapeake Bay, April – June 2003.

K490 April - June 2002

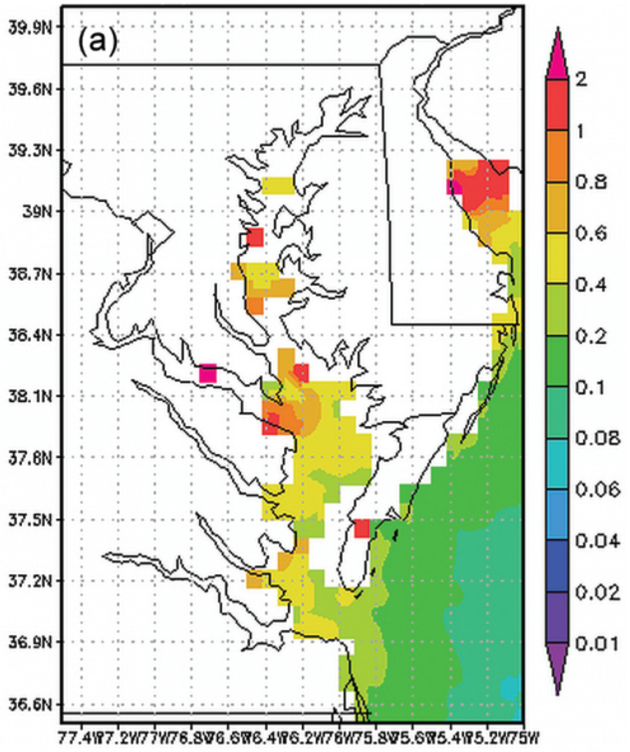

K490 April - June 2003

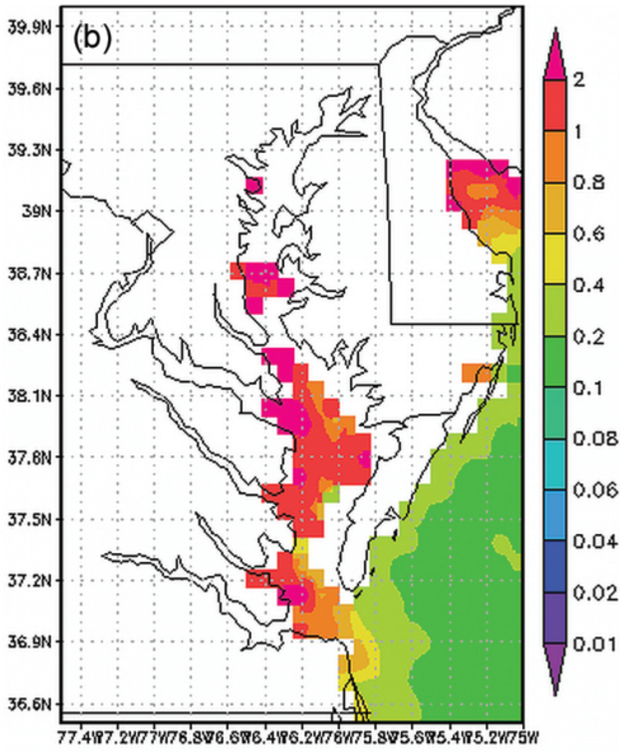

Figure 1.4 (a) Average K490 in the Chesapeake Bay, April – June 2002 (b) Average K490 in the Chesapeake Bay, April – June 2003.

Q 12: What are the likeliest causes of the elevated values of K490 in the Chesapeake Bay, and what is the potential relationship to stream-flow and the transport of fresh water into the Bay?

The next pair of images to examine is the pair of $R_{rs}555$ maps of the Chesapeake Bay. You will again examine the two maps side-by-side. Figure 1.5a depicts $R_{rs}555$ during April – June 2002, and Figure 1.5b depicts $R_{rs}555$ during April – June 2003.

Q 13: During which period are the $R_{rs}555$ values in the Bay significantly higher?

Q 14: Does this period of time correspond to the period when precipitation in the Chesapeake Bay watershed region was low (January – September 2002) or high (October 2002 – June 2003)?

Q 15: The answer to the previous question may be surprising. Given what you have determined about the bio-optical conditions in the Chesapeake Bay from the previous two pairs of maps (for chl-*a* and K490), what is the likeliest explanation for the relationship between $R_{rs}555$ and stream-flow during periods of high and low precipitation?

The final images that will be examined are the impervious surface maps of the Chesapeake Bay region and urban areas within this region (Figures 1.6 to 1.8) and supplemental material entitled "Breath of Life" (see `http://www.eco-check.org/pdfs/do_letter.pdf`).

Q 16: What do you think would be the effects of increasing areas of impervious surface in the watershed of the Chesapeake Bay on the water conditions in the Bay? (Consider the effects on water clarity, water chemistry, bottom visibility, nutrient concentrations, and phytoplankton productivity.)

1.5 Answers

A 1: The average daily precipitation during this period was 1.9 – 2.6 mm day^{-1}.

A 2: The approximate total precipitation during this period was 500 – 700 mm.

A 3: The average daily precipitation during this period was 3.2 – 3.8 mm day^{-1}.

A 4: The approximate total precipitation during this period was 860 – 1030 mm.

A 5: The markedly different rainfall amounts would result in significant differences in the volume of water flowing in the streams and rivers. During the low precipitation period, stream-flow would be significantly reduced. During the high precipitation period, stream-flow would be considerably greater than during the low precipitation period.

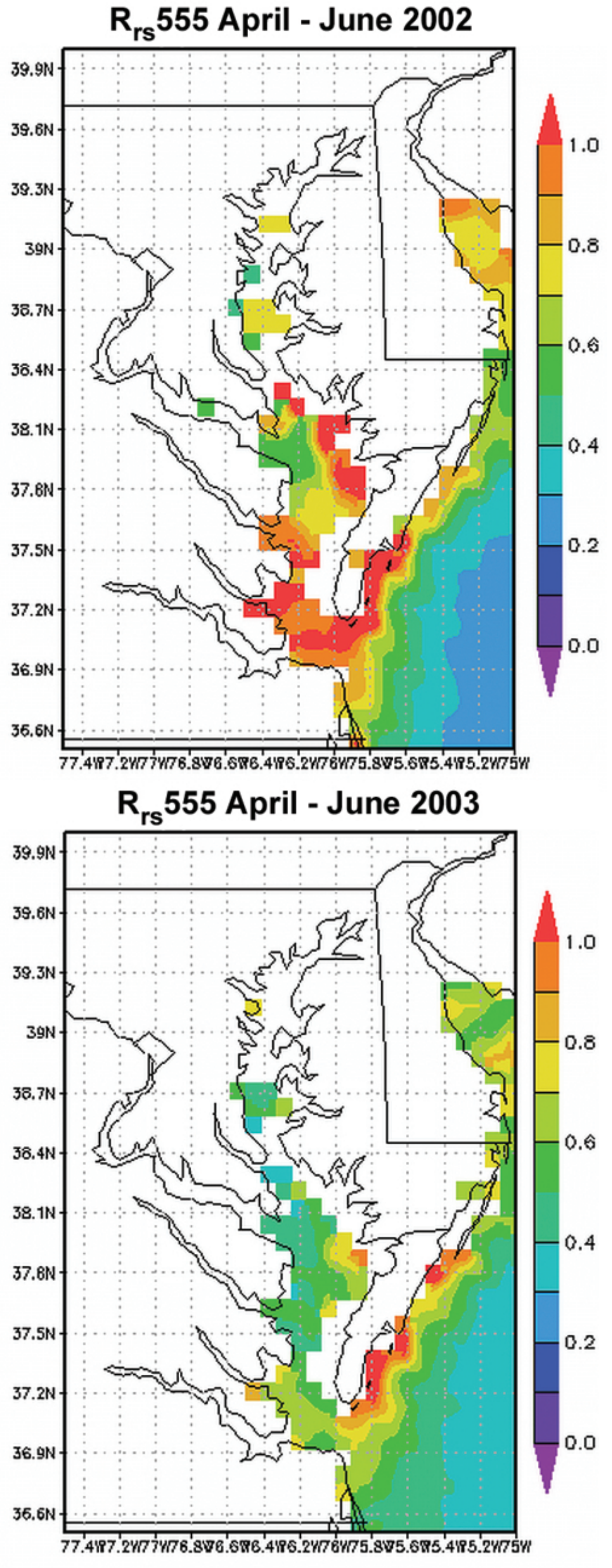

Figure 1.5 (a) Average $R_{rs}555$ in the Chesapeake Bay, April – June 2002 (b) Average $R_{rs}555$ in the Chesapeake Bay, April – June 2003.

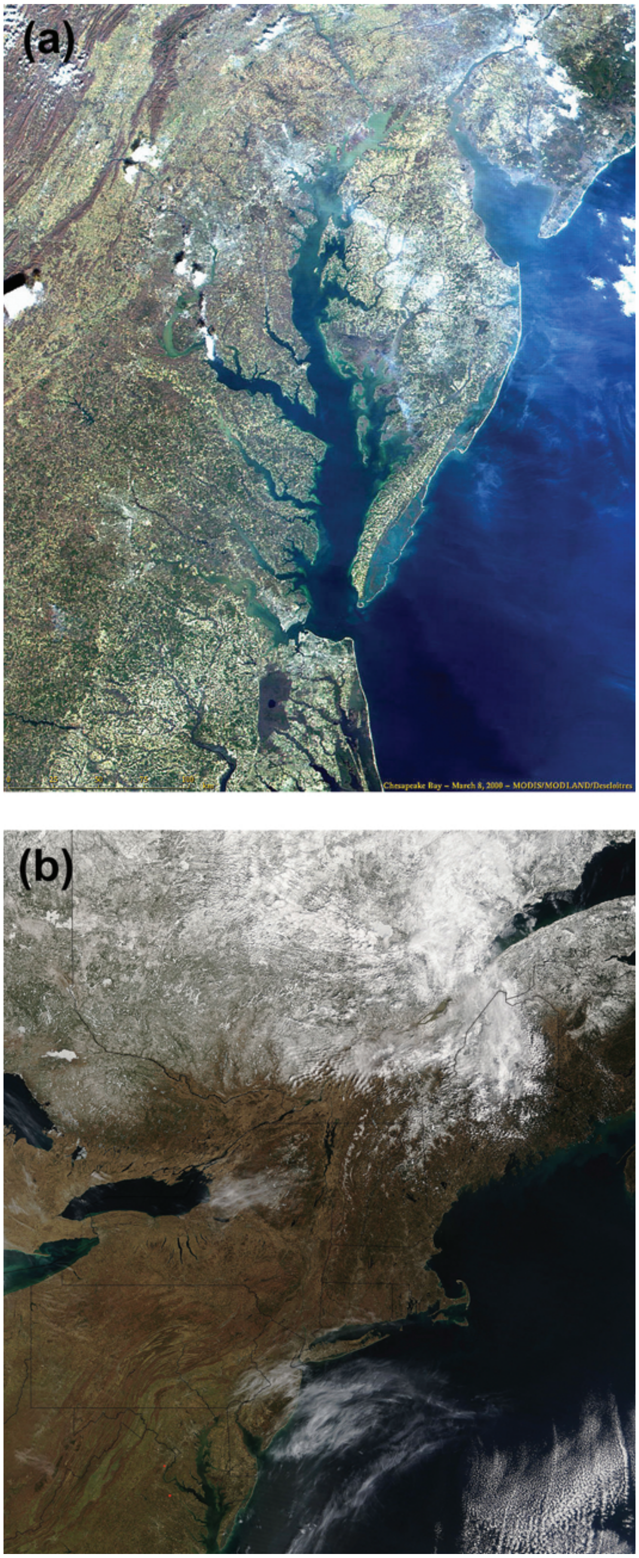

Figure 1.6 (a) MODIS image of the Chesapeake Bay, acquired 20 April 2000 (b) MODIS image of the Chesapeake Bay watershed, acquired 16 April 2006.

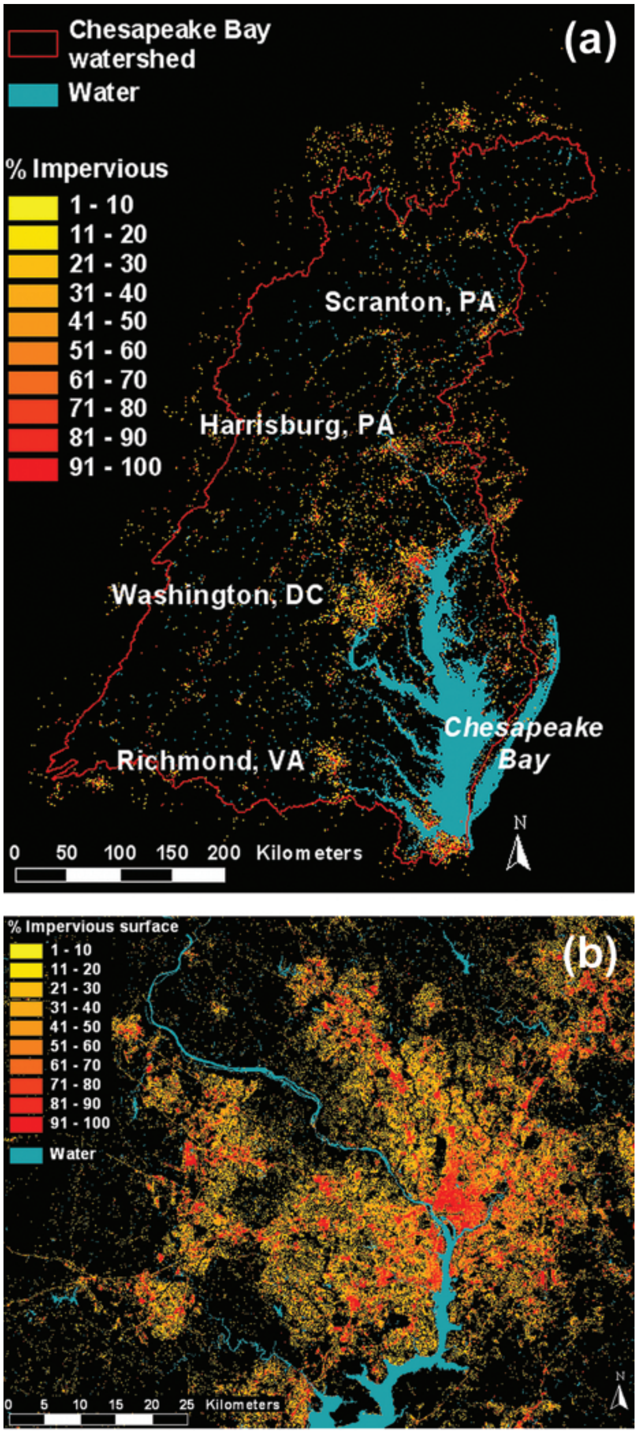

Figure 1.7 (a) Percent impervious surface area in the Chesapeake Bay watershed (b) Percent impervious surface area in the Washington, DC metropolitan area.

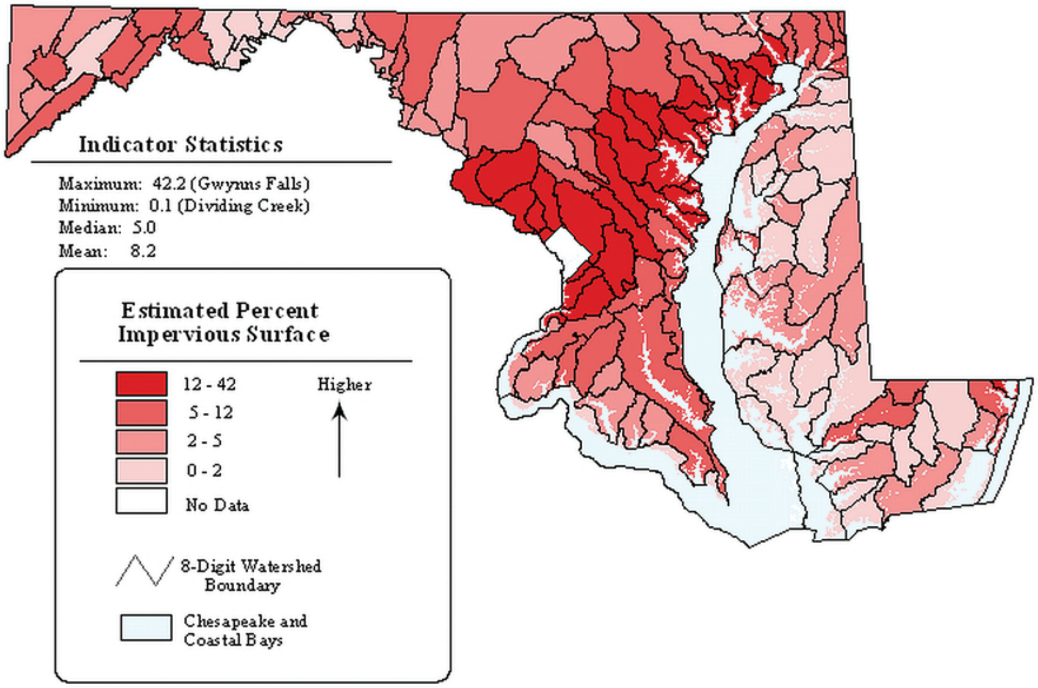

Figure 1.8 Estimated percent impervious surface area in the state of Maryland.

A 6: Due to the increased stream-flow during the high precipitation period, a significantly larger volume of fresh water would enter the Chesapeake Bay, compared to the low precipitation period.

A 7: Chl-*a* values in the Chesapeake Bay are higher during the April 2003 – June 2003 period.

A 8: This period of time corresponds to the period when precipitation in the Chesapeake Bay watershed was high.

A 9: The higher values of chl-*a* corresponding to the period of high precipitation indicate that elevated stream-flow and increased transport of fresh water into the Chesapeake Bay may enhance phytoplankton productivity. This could also be due to increased turbidity (some of which could be more phytoplankton cells in the water). The possible causes are an increased delivery of nutrients in the elevated stream-flow entering the Bay, and also an increased concentration of suspended sediments carried by higher stream-flow volumes.

A 10: The K490 values in the Bay are significantly higher during the April – June 2003 period.

A 11: This period of time corresponds to the period when precipitation in the Chesapeake Bay watershed was high, October 2002 – June 2003.

A 12: The likeliest causes of the elevated values of K490 are directly related to the answer to Question 9. Increased concentrations of phytoplankton and higher concentrations of suspended sediments (and also coloured dissolved organic matter) will all contribute to enhanced light attenuation in the water column. This is the likeliest reason that higher stream-flow and transport of freshwater into the Bay are correlated with higher K490 values.

A 13: The $R_{rs}555$ values in the Bay are significantly higher during the period April – June 2002.

A 14: This period of time corresponds to the period when precipitation in the Chesapeake Bay watershed was low, January – September 2002.

A 15: The surprising result should be related to the difference in the values of chl-*a* and K490 during the high precipitation (high stream-flow) and low precipitation (low stream-flow) periods. Light attenuation is caused by light absorption, light scattering, and light reflection. When the chl-*a* and K490 values are elevated, there are more substances and particles in the water column; thus, the scattering, absorption and reflection of light increases. Simply put, the water is less clear. During the low precipitation/low stream-flow period, the water in the Bay was clearer – and in the shallow depths of the Bay, this allowed more reflection from the bottom of the Bay, which is the likeliest explanation for the increased values of $R_{rs}555$ during the low precipitation period.

A 16: Increased areas of impervious surface will increase both the volume of water entering the Bay at one time during high precipitation events, and will also deliver more undiluted water running off other types of surfaces, such as the lawns of homes or cleared fields. The increased areas of impervious surface can also contribute to erosion when flow volumes are elevated and cause flooding. All of these effects contribute to greater flow of nutrients into the Bay, and can enhance the concentrations of suspended sediments during certain times. These effects will enhance phytoplankton growth and cause decreased water clarity, which affects the survivability of benthic vegetation. Further, the increased growth of phytoplankton leads to increased organic matter deposition on the bottom, causing more bacterial respiration and the spread of areas of low oxygen or no oxygen (hypoxia/anoxia) in the bottom waters of the Bay. In the web document at `http://www.eco-check.org/pdfs/do_letter.pdf` there is a chart (Figure 1.6) of dissolved oxygen levels in the Bay from 1985 – 2006. Note the difference between 2002 and 2003 in this chart. Due to the extremely low stream-flows in 2002, that year was the best overall, in terms of hypoxic and anoxic areal extent, for the entire 22-year period charted.

1.6 References

Acker JG and Leptoukh G (2007) Online analysis enhances use of NASA earth science data. Eos, Trans Am Geophys Union 88(2): 14 and 17

Acker J G, Harding L, Leptoukh G, Zhu T, and Shen S (2005) Remotely-sensed chl a at the Chesapeake Bay mouth is correlated with annual freshwater flow to Chesapeake Bay. Geophys Res Lett 32: L05601. doi:10.1029/2004GL021852 01

O'Reilly JE, Maritorena S, Siegel D, O'Brien MC, Toole, D, Mitchell BG, Kahru, M, Chavez FP, Strutton P, Cota G, Hooker SB, McClain CR, Carder KL, Muller-Karger F, Harding L, Magnuson A, Phinney D, Moore GF, Aiken J, Arrigo KR, Letelier R, and Culver M (2000) Ocean color chlorophyll a algorithms for SeaWiFS, OC2 and OC4: Version 4. In: Hooker SB and Firestone ER (eds) SeaWiFS Postlaunch Calibration and Validation Analyses (Part 3), NASA Technical Memorandum 2000-206892, Volume 10, NASA GSFC, 9-23

Mueller JL and Trees, CC (1997) Revised SeaWiFS prelaunch algorithm for the diffuse attenuation coefficient K(490). In: Yeh, E-n, Barnes RA, Darzi M, Kumar L, Early EA, Johnson BC, Mueller JL and Trees, CC (eds) Case Studies for SeaWiFS Calibration and Validation, E-n. Yeh, R. A. Barnes, M. Darzi, L. Part 4, NASA Tech. Memo. 104566, NASA Goddard Space Flight Center, Greenbelt, Md., Volume 41

Case Study 2

Detection of Oil Slicks using MODIS and SAR Imagery

Chuanmin Hu^{*1}**, Xiaofeng Li**^{2}**, William G. Pichel**^{3}

2.1 Background

Oil pollution can cause extensive damage to marine and terrestrial ecosystems. Every year, huge quantities of oil and petroleum products enter the sea, land, and groundwater (NAS, 2003). The pollution can come from a variety of sources, including leakage from oil transportation, accidents on oil platforms, atmospheric deposition, and seepage from natural seeps. Timely and accurate detection of oil pollution in the ocean can help management and research efforts, yet it is often a difficult task due to limited technical means in monitoring the vast ocean.

Remote sensing provides rapid, frequent, and synoptic measurement of the ocean's surface waters, and thus has been used widely to monitor oil pollution at sea, as well as in lakes. The remote sensing instruments include optical, microwave, and radar (e.g., synthetic aperture radar, SAR) sensors which can be equipped on both aircrafts and satellites. Each of the instruments and measurement platforms has its own advantages and disadvantages (Fingas and Brown, 1997; 2000; Brekke and Solberg, 2005). While airborne remote sensing offers the highest resolution (i.e., the sharpest image) and fastest response to a pollution event, it is often too expensive to be used for operational monitoring. In contrast, satellite remote sensing provides more frequent measurements of the ocean, hence more suitable for oil pollution monitoring.

Among the various satellite instruments, SAR is perhaps the most often used for oil detection at sea. The sea-surface backscattered radar signal is modulated by the wind-induced capillary waves, and thus carries information on the surface roughness. An ocean surface oil film has higher surface tension than water, and can dampen the surface capillary waves, resulting in a smoother sea surface. This in

---

[1] College of Marine Science, University of South Florida, 140 7th Ave., S., St. Petersburg, FL 33701, USA. **Email address:* `hu@marine.usf.edu`

[2] IMSG, NOAA NESDIS, USA

[3] NOAA NESDIS, USA

turn reduces the backscattered radar signal, making oil contaminated areas appear as dark patches in SAR images.

Because radar signals can "penetrate" clouds, SAR images are cloud free and efficient for detecting the various ocean surface features. However, routine application of SAR data is limited by its high-cost and narrow satellite swath (i.e., spatial and temporal coverage). Depending on the measurement mode, measurement of the same place can require days to weeks. These factors make it desirable to seek alternatives to complement SAR observations.

There are currently several Sun-synchronous, polar-orbiting satellite ocean-colour instruments that can measure the ocean's bio-optical properties every day. These include the Sea-viewing Wide Field-of-view Sensor (SeaWiFS, 1997 - present; McClain et al., 2004), the MODerate resolution Imaging Spectroradiometer (MODIS, 1999 - present for Terra, and 2002 - present for Aqua; Esaias et al., 1998), and the Medium Resolution Imaging Spectrometer (MERIS, 2002 - present). While MERIS was launched by the European Space Agency (ESA), SeaWiFS and MODIS are supported by the U.S. NASA. Global data are available for free downloading in near real-time. In particular, MODIS is equipped with several 250-m and 500-m resolution bands, representing a significant enhancement over the present coastal observation capability for the international community. The combined MODIS-Terra and MODIS-Aqua missions cover the global ocean in any single day, thus providing great potential to develop ocean applications.

Hu et al. (2003) used MODIS 250-m resolution data to detect and monitor oil spills in a turbid lake in Venezuela. After removing clouds, two images per week were obtained at no cost. The detection was possible because the high turbidity of the lake water provided a "bright" background where the highly light-absorbing oil films could be visualized. In the oligotrophic ocean, the water background is also dark, making oil detection difficult. However, Hu et al. (2009) showed that when MODIS imagery contained sun glint (i.e., specular reflection of the solar beam), high contrast was found between oil slicks and the background water. The contrast is not due to the difference in optical properties of the oil film and the water (as evidenced by the lack of contrast in other glint-free images), but due to the oil-modulation of the surface capillary waves - the same principle for SAR measurements. Indeed, the ability of visible imagery (including those from space shuttle photos) over sun glint regions to serve as effective radar signals was recognized decades ago and demonstrated recently using satellite imagery (Chust and Sagarminaga, 2007). However, its routine application has been difficult due to lack of near-daily data. The free availability of MODIS daily data for the global oceans makes it possible to implement a cost-effective means for oil spill monitoring.

Here, using MODIS 250-m resolution imagery and RADARSAT-1 SAR 25-m resolution imagery, we show several examples of how oil slicks are identified and interpreted. Three case studies are presented here. The first covers the western Gulf of Mexico (GOM, 18° – 31°N, 98° – 81°W) where numerous oil seeps exist. The second covers the NE GOM where a tragic oil spill event began on 20 April 2010. The last example covers the East China Sea (ECS, 25° – 35°N, 120° – 130°E) where oil pollution from terrestrial and ship discharges is well known.

2.1.1 Data Source and Processing Methods

SAR data from RADARSAT-1 (C-band radar with horizontal polarization and 100-km swath width) were obtained during the Alaska SAR Demonstration (AKDEMO) project. These 25-m resolution images were standard beam mode scenes, processed at the Alaska Satellite Facility (ASF) at the University of Alaska, Fairbanks. The images provided relative intensity of the SAR signal (in digital numbers), and were navigated and analyzed using the software ENVI (Environment for Visualizing Images, version 4.2). The geo-referenced (or map-projected) digital images were stored in PNG graphical format.

All MODIS data were downloaded from the NASA Goddard Space Flight Center (GSFC) at no cost (`http://oceancolor.gsfc.nasa.gov`). These data are open to the public in near real-time and do not require data subscription. The following steps were used to generate geo-referenced MODIS images at 250-m resolution.

1. MODIS Level-0, 5-minute granules, were downloaded from NASA/GSFC;
2. MODIS Level-0 data were processed to generate Level-1b (calibrated total radiance) data for the 36 spectral bands using the SeaWiFS Data Analysis System (SeaDAS version 5.1). The Level-1b data were stored in computer files in HDF (Hierarchical Data Format);
3. MODIS Level-1b data were corrected for gaseous absorption (ozone and other gases) and Rayleigh scattering effects, resulting in the Rayleigh-corrected reflectance:

   $$R_{\mathrm{rc},\lambda}(\theta_0, \theta, \Delta\phi) = \pi L_{\mathrm{t},\lambda}{}^*(\theta_0, \theta, \Delta\phi)/(F_0\lambda) \times \cos\theta_0) - R_{\mathrm{r},\lambda}(\theta_0, \theta, \Delta\phi) \quad (2.1)$$

   where λ is the wavelength for the MODIS band, $L_{\mathrm{t}}{}^*$ is the calibrated sensor radiance after correction for gaseous absorption, F_0 is the extraterrestrial solar irradiance, θ_0 is the solar zenith angle, θ is the sensor (viewing) zenith angle, $\Delta\phi$ is the relative azimuth between the sun and the satellite, and R_{r} is the reflectance due to Rayleigh (molecular) scattering. The solar-viewing geometry is defined by $(\theta_0, \theta, \Delta\phi)$, which changes from pixel to pixel. This step used the software CREFL from the University of Wisconsin (Liam Gumley). The R_{rc} data of 7 MODIS bands (469, 555, 645, 859, 1240, 1640, and 2130 nm) were stored in HDF computer files. Figures 2.1a and b show examples of the R_{rc} Red-Green-Blue images using 645, 555, and 469-nm as R, G, and B, respectively. If two consecutive 5-minute granules were required to cover the study region, the Level-0 data were combined together before Step 2 was performed;
4. The R_{rc} data were geo-referenced to a cylindrical/equidistance (rectangular or geographic lat/lon) projection for the area of interest, defined by the

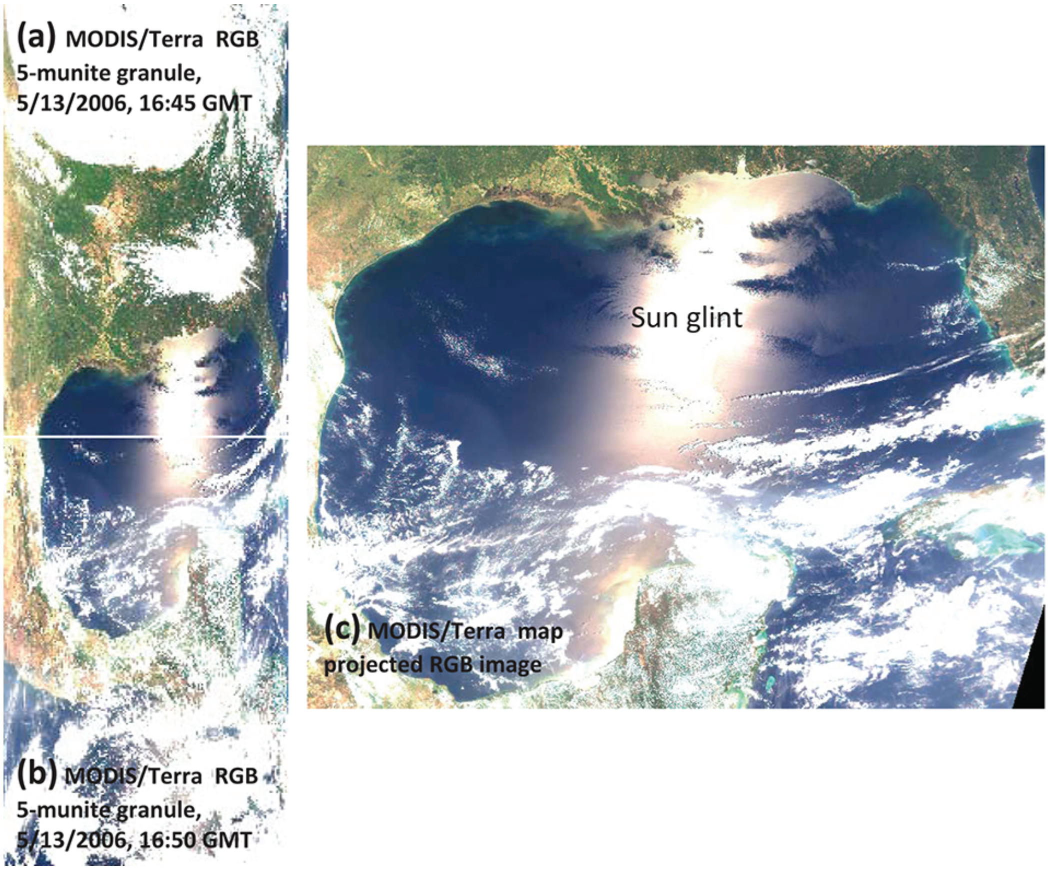

Figure 2.1 Map projection of the MODIS Level-1b R_{rc} data. (a) and (b): two consecutive MODIS/Terra 5-minute granules on 13 May 2006. Each granule contains R_{rc} data at 645 and 859 nm with a dimension of 5416 x 8120, and R_{rc} data from other bands (469, 555, 1240, 1640, and 2130 nm) with a dimension of 2708 x 4060. The RGB images were composed of R_{rc} at 645 (R), 555 (G), and 469 nm (B). (c): rectangular projection of the two granules to cover the area of interest (Gulf of Mexico, from 18° to 31°N and 98° to 81°W). There are 440 image pixels per degree, corresponding to about 250-m per pixel.

North-South and East-West bounds. Because 1 degree is about 110 km, the map-projected data have 440 image pixels per degree, corresponding to 250 m per image pixel. Although only the MODIS 645- and 859-nm bands have a nadir resolution of 250 m, other bands at 500-m resolution were interpolated to 250-m resolution using a sharpening scheme similar to that for Landsat. The mapping software was written in-house using C++ and PDL (Perl Data Language) with an accuracy of about 0.5 image pixel;

5. The map projected R_{rc} data at 645, 555, and 469 nm were converted to byte values using a linear stretch (coefficients determined by trial-and-error), and then used as the red, green, and blue (RGB) channels, respectively, to compose a RGB image. Figures 2.1c shows the map projected RGB image at 250-m

resolution from the combined 5-minute granules in Figures 2.1a and b;
6. The RGB image was loaded in the software ENVI for display and analysis.

2.2 Demonstration

Because of the synoptic coverage (often >10 degrees in both N-S and E-W directions) and medium resolution (250-m per pixel), the MODIS RGB image is very large (e.g., the dimension of Figure 2.1c is 7480 × 5720 pixels). Further, the colour stretch is compromised to cover both sensitivity (the smallest difference between pixels) and dynamic range (the lowest and highest pixel values). Thus, interactive stretching and zooming functions are required to visualize the various image features. While several commercial software packages (e.g., ArcInfo or Erdas Imagine, or any other software that has basic image processing capabilities) can be used, we use the software ENVI to demonstrate how the oil-like features are identified.

First, the RGB image is loaded into ENVI by using the "File → Open Image File" function. Three display windows are shown (Figure 2.2 top panels): scroll, image, and zoom. The scroll window shows the entire region at reduced resolution to serve as a browse image; the image window shows a portion of the image at full resolution (250-m); and the zoom image enlarges a smaller portion by 4 times.

During the initial display in ENVI, the colours are stretched linearly from 0 to 255 to cover the entire image. This often makes the subtle surface features invisible. The image window is thus colour enhanced by a "Gaussian" enhancement, using the menu of "Image → Enhance → Gaussian". The result is that the image window is colour enhanced, at the price of either over-stretching or under-stretching for other regions. The various image panels in Figure 2.2 show the before-after comparison using the Gaussian enhancement.

What are the identified dark slicks in Figure 2.2? SAR data collected on the same day in an adjacent region showed identical features to those appearing in the corresponding MODIS image (Figure 2.3). Further, the MODIS image for the region in Figure 2.3 contains low to moderate sun glint (Hu et al., 2009), and another MODIS image collected 3 hours later over the same region, but without sun glint, shows no features at all. All this combined evidence suggests that these dark features are indeed due to dampened surface roughness and not due to changes in water's optical properties.

Several other processes, in addition to oil films, can lead to reduced surface roughness. These include phytoplankton or fish induced surface surfactant, shoals, and coastal freshwater jets (Alpers and Espedal, 2004). The region shown in Figure 2.3 is located in an oligotrophic ocean away from land, so these potential processes can be ruled out. The most striking evidence is that these features are recurrent in the same place, and they can also be observed in other images under optimal conditions (cloud free, with some degree of sun glint). Figure 2.4 shows two other examples, both using ENVI's Gaussian enhancement, where the slicks from two different days appear to have a one-to-one relationship and originate from the same locations. They are oriented differently due to different surface currents and winds. The only explanation, then, is that these surface slicks are oil films from oil seeps on the ocean floor. Indeed, the NW GOM is well known to have numerous oil seeps and previous studies using a variety of methods (including remote sensing) confirmed the existence of oil seeps (McDonald et al., 1993; 1996). Thus, even without *in situ* validation, we can conclude that these surface features are indeed oil slicks floating on the surface.

This application is further demonstrated using MODIS imagery to examine a recent tragic oil spill event. On 20 April 2010, an explosion occurred on the oil drilling rig, the Deepwater Horizon, in the northern GOM (28.74°N, 88.37°W). After burning for a day, the rig sank to the 1500-m ocean floor, resulting in the largest oil spill event in the U.S. history. The main cause of the spill was a continuously leaking oil well, with estimates of at least 5,000 barrels per day (indeed, later estimates by several independent groups showed up to 50,000 barrels per day). Various methods have been used to assess the volume, fate, and trajectory of the spilled oil to help mitigate the potential adverse impacts on ocean and terrestrial ecosystems. Using the principles shown above, we processed and provided MODIS imagery in near real-time to the management agencies and researchers, and made them available online in Google-Earth compatible format to facilitate visualization and tracking of the spill (`http://optics.marine.usf.edu/events/GOM_rigfire`, Figure 2.5). In Figure 2.5b it can be seen that among the scattered clouds there is a suspicious feature. The feature appears like clouds, but its spectral shape is noticeably different from clouds, with relatively lower reflectance in the blue wavelengths due to enhanced Rayleigh scattering along the sun glint beam (the same principle behind why sunset is reddish). The sun glint reflectance and viewing angle (relative to the mirror direction of the sun) were estimated as 0.048 sr^{-1} and 12.6°, respectively. Further, the spatial shape and lack of shadow also indicate that the suspicious feature is oil. Figures 2.5c and d show two other examples from the same day from MODIS-Terra and MODIS-Aqua observations, respectively. Due to changes in the solar/viewing geometry, the same oil slicks show positive contrast in the morning but negative contrast in the afternoon, agreeing with what has been observed from natural oil slicks in the GOM (e.g., Figure 2.4).

Note that the reason for using RGB images instead of individual MODIS bands (e.g., 859 nm) is that clouds and cloud shadows can be easily visualized and ruled out as potential oil slicks.

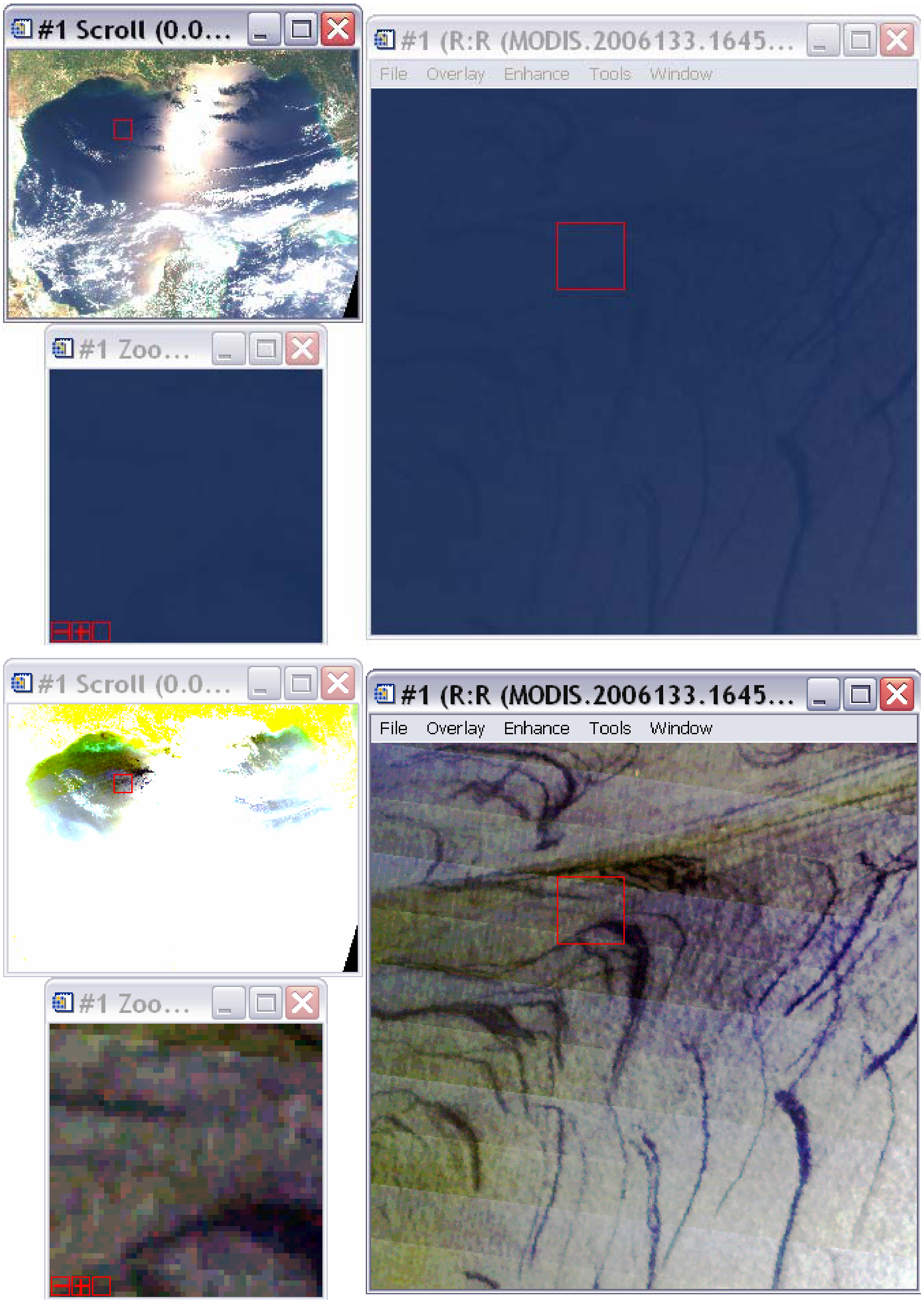

Figure 2.2 Interactive colour stretching within the software ENVI is used to enhance the contrast between the oil-like features and the background water. Top: original RGB image in scroll (upper left), image (upper right), and zoom (bottom left) display windows. Bottom: the same image after Gaussian enhancement. Similar enhancement can be performed in other software packages.

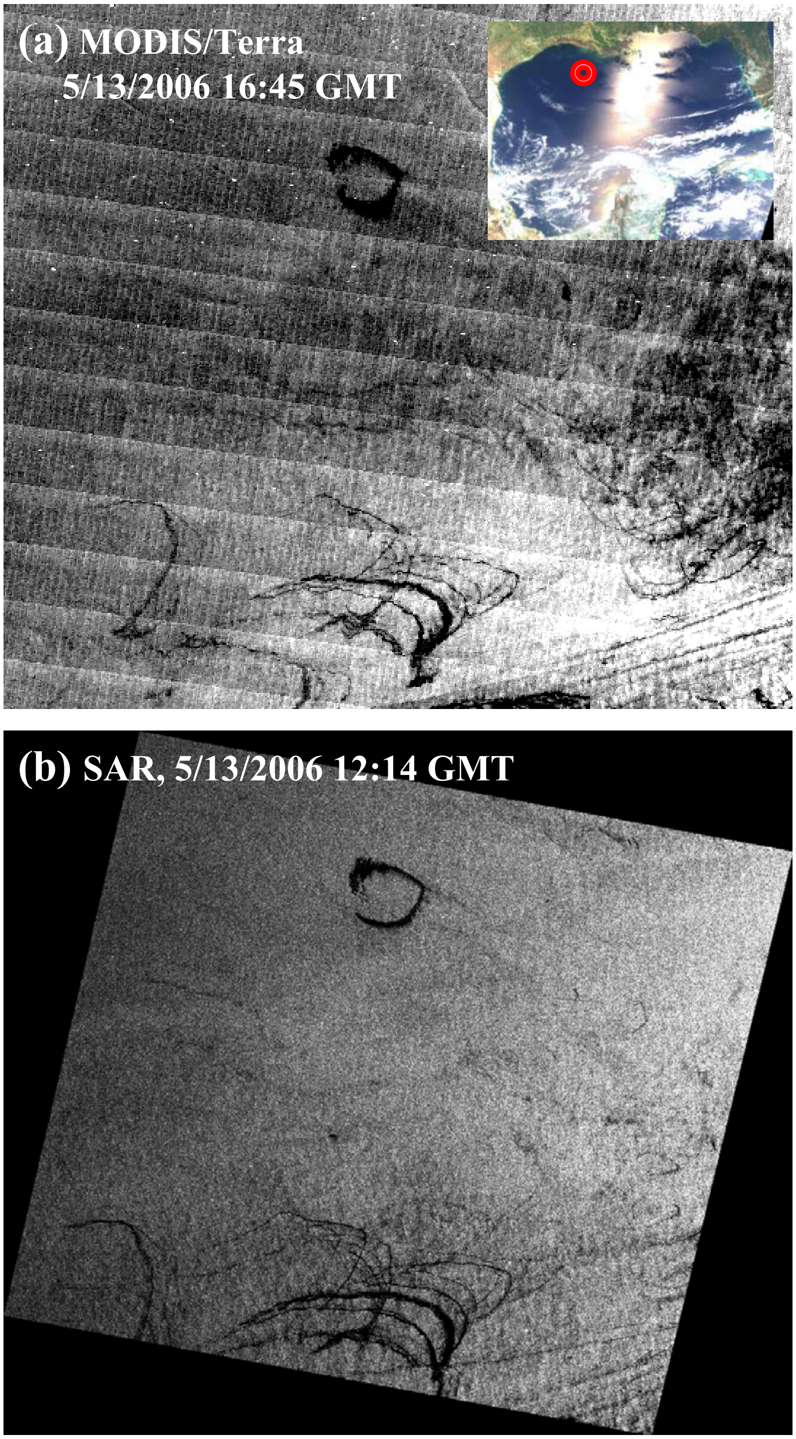

Figure 2.3 MODIS/Terra image (a) and SAR image (b) showing oil slicks in the NW Gulf of Mexico (inset MODIS Red-Green-Blue figure) between 27.38° to 28.48°N and 93.25° to 92.01°W. The data were collected 4.5 hours apart, yet the slick patterns appear identical. The MODIS image was coloured stretched in ENVI using Gaussian enhancement.

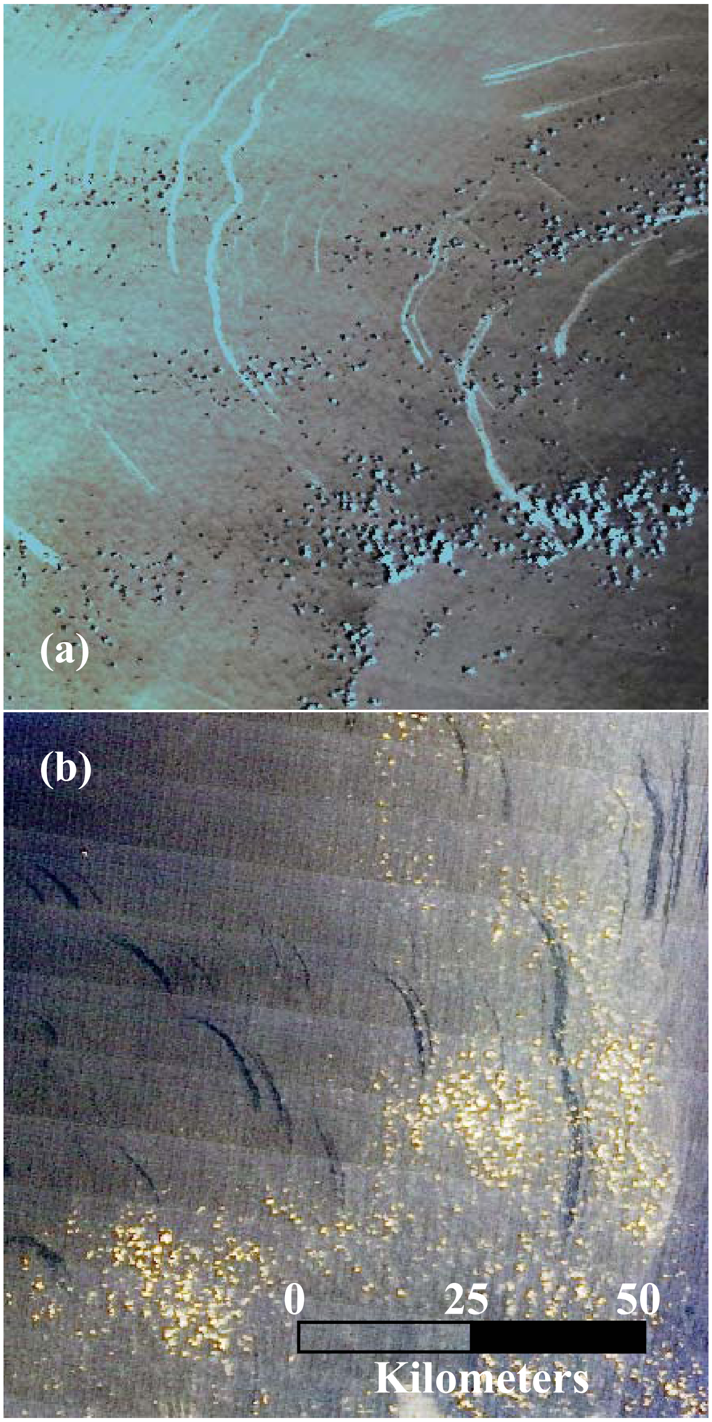

Figure 2.4 MODIS/Terra images collected on 5/13/2001 (a) and 5/24/2001 (b) showing oil slicks in the NW Gulf of Mexico as positive and negative contrasts, respectively, against the background. The contrast change is due to different solar/viewing geometry in the sun glint patterns (Hu et al., 2009).

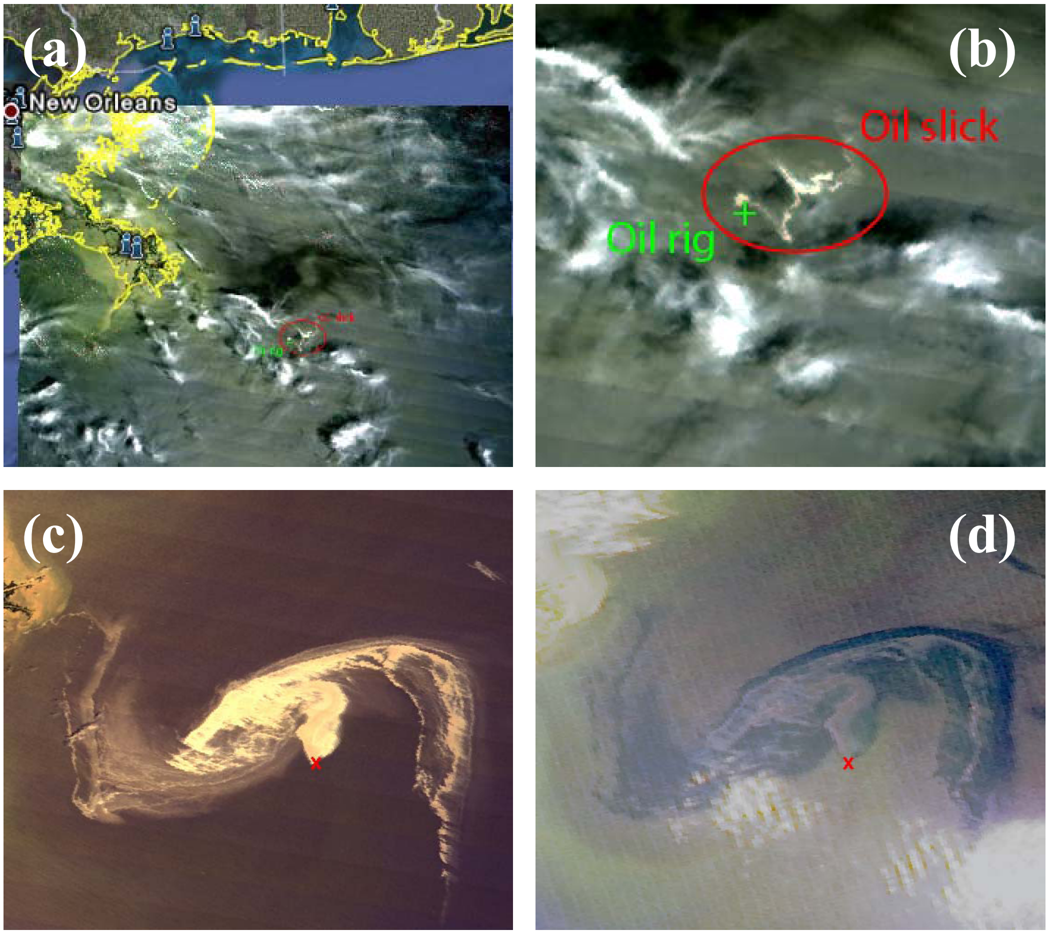

Figure 2.5 MODIS images showing oil slicks in the northern Gulf of Mexico due to oil spills from a sunken oil rig (the Deepwater Horizon) on 20 April 2010. The location of the oil rig is marked with a cross. (a) MODIS image on 22 April 2010 overlaid on a Google-Earth map shows that the oil rig is approximately 40 km southwest of the Mississippi River mouth near New Orleans, Louisiana, U.S.A. (b) An enlarged image shows the oil slick and the surrounding clouds. (c) MODIS image on 29 April 2010 (16:55 GMT) shows the oil slicks in positive contrast. (d) MODIS image on the same day but at 18:30 GMT shows the same oil slicks in negative contrast. The horizontal scale of (b)-(d) is about 120 km. More images are available at `http://optics.marine.usf.edu/events/GOM_rigfire`.

2.3 Training and Questions

Three MODIS RGB images are provided on the IOCCG website (`http://www.ioccg.org/handbook/Hu_oil/`) to help identify oil slicks and oil-like features. The first two cover the GOM, collected on 13 and 24 May 2001 by MODIS-Terra. The third image covers the ECS (25 to 35°N, 120 to 130°E), collected by MODIS-Aqua on 18 July 2008. The visualization and analysis can be performed in the following steps. We use

ENVI to describe the steps, but any other software package that has basic image processing capabilities can also be used.

1. Open the two MODIS images in ENVI. Use the "Tools → Link → Link Displays" to link the two images, so that they both show the identical region at the same time. By clicking on one image and toggling "on-off", the other image is co-registered and shown on top of the current image. This way, it is easy to identify whether certain features on the two images originate from the same locations;
2. Move the image window to the NW GOM, and use the Gaussian enhancement to enhance the colour contrast. Repeat this until a satisfactory enhanced image is obtained. This step should result in two images similar to those shown in Figure 2.4.

The second exercise is to explore the MODIS image covering the ECS. Using the interactive Gaussian stretch in ENVI, a colour-enhanced image should be obtained to show dark slicks and patches near the Yangtze River estuary in the sun glint region (Figure 2.6).

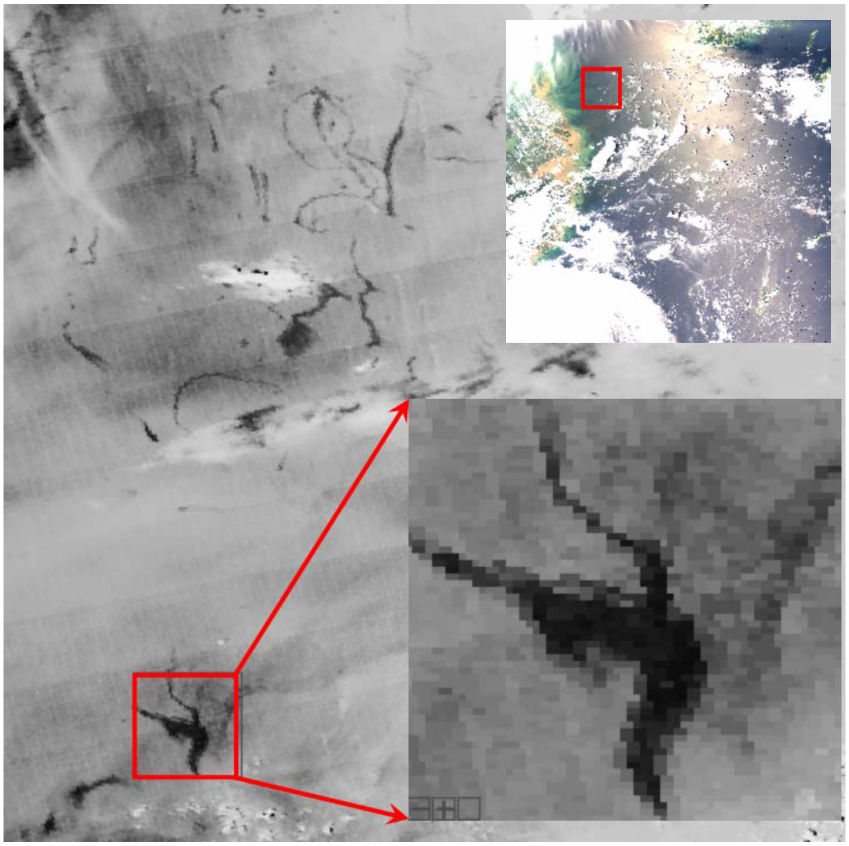

Figure 2.6 MODIS image showing surface features that appear to be oil slicks in the East China Sea (ECS). Inset: MODIS Red-Green-Blue figure covering 25 to 35°N and 120 to 130°E on 7/18/2008 04:40 GMT.

2.4 Questions

Q1: Why are the slicks brighter than the surrounding water (i.e., positive contrast) in Figure 2.4a?

Q2: Is there a one-to-one relationship between the bright slicks (Figure 2.4a) and dark slicks (Figure 2.4b), and do they have the same origins?

Q3: Are these dark features in Figure 2.6 oil films? If so, where do they come from?

2.5 Answers

A1: Crude oil from oil seeps strongly absorbs light and therefore should appear darker than the adjacent waters. Then, why are the slicks in Figure 2.4a brighter? Using MODIS data and sun-glint estimates based on solar/viewing geometry and surface wind, Hu et al. (2009) demonstrated that if the satellite views the region close to the "mirror direction" of the sun (< 12-14°), positive (i.e., brighter) contrast can result from enhanced specular reflection by the oil film. Thus, depending on how the region is viewed by the satellite (relative to the sun), the oil slicks can show no contrast (in glint-free imagery), negative contrast (low to moderate sun glint) or positive contrast (strong sun glint) in MODIS imagery. The same positive contrast is also observed in Figure 2.5a.

A2: The ENVI "Link Displays" function provides an excellent tool for tracing features on two different images. By clicking on one image with the other toggled on or off, one can easily visualize that the bright and dark slicks have a one-to-one relationship and that they indeed have the same origins. The slight difference in the traced origins between the two different days should be due to the horizontal movement during the upwelling of the bottom oil (from 1 – 2 km deep). Nevertheless, the rough locations can significantly narrow down the search range when *in situ* operations are used to locate the exact locations of the oil seeps.

A3: It is well known that the ECS, particularly the western part, is subject to oil pollution from a variety of sources, including land-based sewage discharge, illegal ship discharge, and oil transportation accidents (Li and Daler, 2004; Shi et al., 2008). Using over 600 SAR images collected over the western ECS between 2002 and 2005, Shi et al. (2008) concluded that most of the oil-like slicks were from ship discharges. The dark features shown in Figure 2.6 are from MODIS sun-glint regions, and they have spatial texture (shape, size, spatial contrast) similar to oil slicks found in MODIS sun-glint imagery in the western GOM. Therefore, in the absence of an *in situ* validation effort, and considering their proximity to the shipping routes, we can conclude that these dark features are very likely oil slicks from ship discharge. Note that without background information or *a priori* knowledge of the study region, the difficulty in recognizing oil slicks from suspicious features also holds true for SAR imagery (Alpers and Espedal, 2004). In this regard, the performance of the MODIS sun-glint imagery in detecting oil slicks is comparable to that of SAR, except that MODIS has a lower resolution (250-m versus 25 or 10-m for SAR) and is restricted by clouds.

2.6 Discussion and Summary

The three case studies demonstrated here (one for natural oil seeps in the western GOM, one for a tragic oil spill event in the eastern GOM, and one for ship or river discharges in the western ECS) clearly show the potential of MODIS imagery in detecting oil slicks in both oligotrophic and turbid ocean waters. In turbid coastal waters where water reflectance is high, observation of oil slicks does not require sun glint, as shown by Hu et al. (2003) for Lake Maracaibo, Venezuela. Likewise, when surface oil slicks are thick, sun glint is not required either (Figure 5d). However, such potential of MODIS should not be over-emphasized compared with other means (e.g., SAR detection) because 1) the MODIS visible and near-IR bands cannot penetrate clouds, and the method is useless for cloud contaminated image pixels; and 2) for oligotrophic oceans and thin slicks, some degree of sun glint is required to detect the changes in surface roughness, and this requirement limits its use in high latitude regions. Finally, when sun glint is required for the observations, all limitations that apply to SAR applications for oil detection (e.g., optimal wind speed, difficulty in differentiating the various dark features) may also apply to MODIS imagery because they are based on the same principles (i.e., changes in surface roughness).

However, MODIS has the advantage of greater coverage and no data cost, thus enabling a potentially quasi-operational system to be implemented for routine applications, and fast response in case of oil spill events. MODIS has a swath width of about 2300 km, and the two MODIS instruments onboard the Terra (morning pass) and Aqua (afternoon pass) satellites make the spatial/temporal coverage at moderate resolution (250-m) unprecedented by any in-orbit satellite instruments. In this regard, for regions with a potential for heavy oil spills, a MODIS-based system could be implemented. Indeed, the most recent oil spill event in the Gulf of Mexico (Figure 5) provides an excellent example as to how a MODIS-based, quasi-operational system can contribute to monitoring and mitigation of oil spills. MODIS provided near daily oil spill coverage for most of the NE GOM during the first month of the spill event (21 April to late May 2010). When cloud cover increased from late May towards the summer, SAR data from several sources were combined with MODIS observations to improve the coverage. The advantage of combining more synoptic and frequent MODIS data with cloud-free SAR data in oil spill monitoring has been clearly demonstrated in this case.

In summary, oil films on the sea surface modulate the surface roughness (capillary/gravity waves), and thus can be differentiated from their surrounding waters in MODIS sun glint imagery. This ability is demonstrated by three case studies where oil slicks from natural seeps, an oil spill accident, and possible ship discharges are identified. When oil films are thick, their optical properties (light absorption and surface Fresnel reflection) can make them well distinguished from the surrounding waters, as shown in the recent GOM oil spill case study. Because of the free availability of the MODIS 250-m data since 2000, a monitoring system at low cost can be established, in principle, for any part of the global oceans where sun glint is frequently observed. Combined with SAR observations, such a system may significantly enhance our capability to monitor oil spills in most of the global oceans. Automated delineation and quantification of oil slicks (e.g., thickness) using texture analysis as well as image segmentation, however, still requires further research.

2.7 References

Alpers W, Espedal HA (2004) Oils and surfactants. In: Jackson CR and Apel JR (eds) Synthetic Aperture Radar Marine User's Manual. U.S. Department of Commerce, Washington, DC, September 2004. pp 263-275

Brekke C, Solberg AHS (2005) Oil spill detection by satellite remote sensing. Remote Sen Environ 95:1-13

Chust G, Sagarminaga Y (2007) The multi-angle view of MISR detects oil slicks under sun glitter conditions. Remote Sens Environ 107:232-239

Esaias WE, Abbott MR, Barton I, Brown OB, Campbell JW, Carder KL, et al. (1998) An overview of MODIS capabilities for ocean science observations IEEE Trans. Geosci Remote Sens 36:1250-1265

Fingas M, Brown C (1997) Remote sensing of oil spills. Sea Technology 38:37-46

Fingas M, Brown C (2000) Oil-spill remote sensing - An update. Sea Technol 41:21-26

Hu C, Muller-Karger FE, Taylor CJ, Myhre D, Murch B, Odriozola AL, Godoy G (2003) MODIS detects oil spills in Lake Maracaibo, Venezuela. EOS, Transactions, AGU, 84(33):313,319

Li D, Daler D (2004) Ocean pollution from land-based sources: East China Sea, China. ABBIO, 33:107-113

MacDonald IR, Guinasso NL, Ackleson SG, Amos JF, Duckworth R, Sassen R, Brooks JM (1993) Natural oil slicks in the Gulf of Mexico visible from space. J Geophys Res 98(C9):16,351-16364

MacDonald IR, Reilly JF, Best SE, Venkataramaiah R, Sassen R, Guinasso N, Amos J (1996) Remote sensing inventory of active oil seeps and chemosynthetic communities in the northern Gulf of Mexico. In: Schumacher D, and Abrams MA (eds) Hydrocarbon migration and its near-surface expression. Am Assoc Petrol Geol Mem. 66:27-37

McClain CR, Feldman GC, Hooker SB (2004) An overview of the SeaWiFS project and strategies for producing a climate research quality global ocean bio-optical time series. Deep-Sea Res II 51:5-42

NAS (2003) Oil in the sea III. Committee on Oil in the Sea: Inputs, Fates, and Effects, Ocean Studies Board and Marine Board, Divisions of Earth and Life Studies and Transportation Research Board, National Research Council. The National Academies Press.

Shi LA, Ivanov YU, He M, Zhao C (2008) Oil spill mapping in the western part of the East China Sea using synthetic aperture radar imagery. Int J Remote Sens 29:6315-6329

Case Study 3

Ocean-Atmosphere Exchanges of Persistent Organic Pollutants on the Atlantic Ocean

Elena Jurado*[1] **Rafael Simó**[2] **and Jordi Dachs**[3]

3.1 Background Information

Persistent Organic Pollutants (POPs), also termed by Persistent Bioaccumulable Toxic chemicals (PBTs), are bioaccumulable compounds of prolonged environmental persistence and are susceptible to long-range atmospheric transport. They have been detected in all the environmental compartments, even in remote areas such as the open ocean and the polar regions, where POPs have never been manufactured or used. Furthermore, once they appear in the environment they do not degrade. Instead, they recycle and partition between the major environmental media, and are an environmental concern since their toxic effects do not disappear, and their control is difficult. Their physicochemical properties, such as the high lipid/organic solubility, result in their bioaccumulation in lipid-rich tissues and 'bio-magnification' through the food chain. Even at low concentrations they are toxic to humans and wildlife, with suspected effects including carcinogenesis, immune dysfunction, neurobiological disorders and reproductive and endocrine disruption.

POPs comprise man-made organo-halogenated compounds (e.g. pesticide POPs such as DDT, industrially produced POPs such as polychlorinated biphenyls (PCBs) or POPs that are unintended byproducts such as polychlorinated dibenzo-p-dioxins and polychlorinated dibenzofurans (PCDD/Fs) and other chemicals that can, in part, be biogenic such as polycyclic aromatic hydrocarbons (PAHs). In particular, man-made POPs were initially produced and used in the 1940s. During the 1960s and 1970s, the use of certain POPs in industry or as pesticides increased dramatically. The first political regulations for the production and use of POPs dates from the late 1970s. Since then, a number of politically-binding regulations have entered into force to reduce or eliminate their emissions: the Convention on Long-Range Transboundary

---

[1] Institute for Marine and Atmospheric Research Utrecht (IMAU), Utrecht University, Princetonplein 5, 3584 CC Utrecht, The Netherlands. **Email address:* `e.juradocojo@uu.nl`

[2] Marine Sciences Institute, CMIMA-CSIC, Passeig Marítim de la Barceloneta 37-49, Barcelona 08003, Spain

[3] Department of Environmental Chemistry, IIQAB-CSIC, Jordi Girona 18-26, Barcelona 08034, Spain

Air Pollution on POPs, the Stockholm Convention on POPs, and, on a European Level, the Water Framework Directive.

Despite regulations, they still cycle between the different environmental compartments and there are non-controlled sources as well. For example, high concentrations of PCBs have been reported in arctic wildlife and breast milk. This is of special concern, not only because those contaminants were already banned in the late 1970s, but also because of the distance from the source where those pollutants were produced. There is thus a global occurrence of these contaminants and an urgent need to control their levels in the environment. Sampling of POPs, however, is time-consuming and expensive compared to many other contaminants. In this context, global models are a very valuable tool to predict and understand the distribution of POPs. Satellite data, with their global synoptic coverage, can provide environmental input data to global POPs models, as we will see later.

To understand how we can use remote sensing data to model the global distribution of POPs, we provide here a short explanation of the partitioning of POPs in the different environmental media. Because both atmosphere and oceans are critical compartments in the global distribution and cycling of POPs, the analysis will focus in the ocean-atmosphere exchanges of POPs. Atmospheric emissions and subsequent long-range transport have proven to provide a mechanism to distribute POPs widely through the global environment. In fact, atmospheric deposition of POPs may be the major process by which they impact remote oceans and other pristine environments. On the other hand, the oceans are also critical in the global cycling of those pollutants; their large volumes imply that they may represent an important inventory of POPs.

Figure 3.1 shows a diagram of the major processes affecting the transfer of POPs between the atmosphere and the ocean. In the atmosphere, POPs partition between the gas and aerosol phases and they may then be removed by three processes: dry deposition of aerosol-bound pollutants, diffusive gas exchange between the atmosphere and the ocean, and scavenging by rain (either from gas or particulate phases), the latter termed wet deposition. In the water column, POPs can be found either dissolved or sorbed to particulate organic matter. Dissolved POPs can revolatilize back to the atmosphere or they can stay in the water column and become bioavailable, i.e. they can be incorporated into the biota by passive diffusion. POPs sorbed to particulate organic matter cannot revolatilize back to the atmosphere, but can be deposited by gravity or sinking. In both particulate and dissolved phases, they are subject to turbulent mixing throughout the water column. Finally, in each medium, POPs are subject to degrade, but those fluxes are generally considered negligible. By means of simplification, no lateral advection of contaminants is considered, which is an assumption generally accepted in the open ocean, where contaminants enter primarily via atmospheric deposition.

The processes affecting the transfers of POPs between the atmosphere and the ocean are evaluated quantitatively by means of fluxes (F [ng m^{-2} s^{-1}]), whose

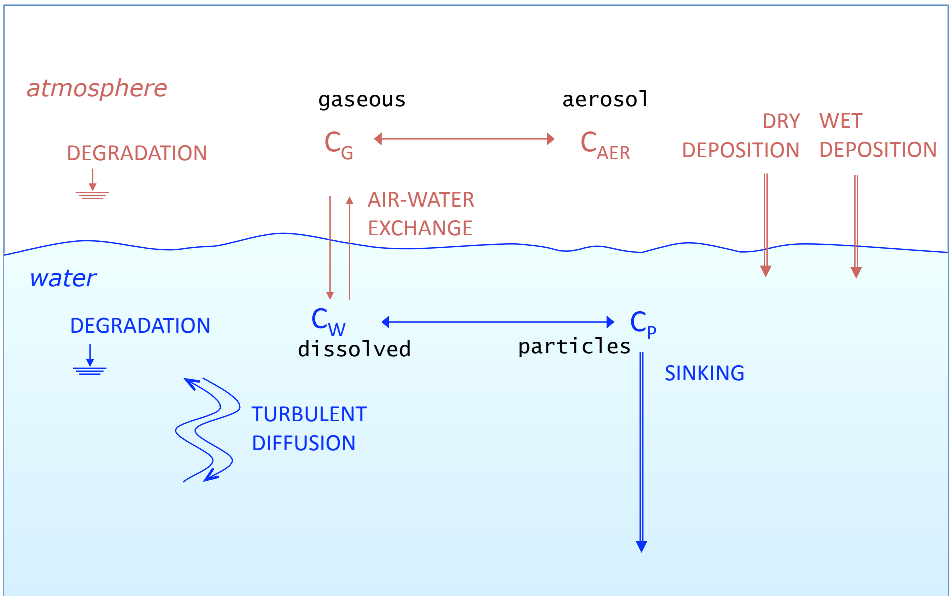

Figure 3.1 Major processes affecting the transfer of POPs between the atmosphere and the ocean. The amount of contaminant in an environmental media is denoted by its concentration, C. Fluxes are marked in capital letters.

simplified mathematical formulation is presented next. Advective processes, where contaminants are transported by means of directed motion, such as dry deposition, wet deposition and sinking, are governed by:

$$F_{\mathrm{advective}} = vC \tag{3.1}$$

where v [m s^{-1}] is the advective velocity and C [ng m^{-3}] is the concentration of the chemical.

Diffusive processes, such as air-water exchange or turbulent flux, where contaminants are transported by random motion, are governed by Fick's First Law:

$$F_{\mathrm{diffusive}} = -D\frac{\partial C}{\partial x} \tag{3.2}$$

where D [m^2 s^{-1}] is the molecular diffusivity and $\partial C/\partial x$ is the gradient of concentrations in the x direction, along which the change of concentration of the contaminant occurs. The mathematical formulation of diffusion becomes more complex if the transport occurs between two media, as would be the case of the diffusive transport across the air-water interface. The resultant flux is then a combination of molecular and turbulent diffusion.

The last type of process, the degradation process, produces a loss in the system, and is characterized by a first order decay rate, k_{degr} [s^{-1}].

$$F_{\mathrm{transformation}} = hk_{\mathrm{degr}}C \tag{3.3}$$

where h [m] is the height of the volume where degradation is acting.

It is important to note that the magnitude of the contaminant fluxes is a function of the measured concentration, physicochemical parameters, and environmental conditions. The environmental conditions do not only determine the parameters v, D and k_{deg}, from Equations 3.1 to 3.3, they also influence the ratio of contaminant concentrations between two different phases of equilibrium. This ratio is termed the *equilibrium partition coefficient* and it is essential in the modelling of POPs. For example, the gas-particle partition coefficient K_p will allow us to calculate the concentration of a certain POP in its aerosol phase, knowing its concentration in the gaseous phase and assuming equilibrium conditions, which is a common assumption since these compounds are continuously seeking to equilibrate between the different reservoirs.

This case-study shows an example of the application of satellite data to estimate the spatial and temporal distribution of atmospheric-ocean fluxes of POPs in the Atlantic Ocean. It has been developed in detail in various publications (Dachs et al. 2002; Jurado et al. 2004; 2005; 2008) and it is based on the previous work of Dachs et al. (2002) and Simó and Dachs (2002). Essentially, satellite retrieved parameters and air measured concentrations (gaseous and aerosol phases) in two north-south campaigns across the Atlantic (Lohmann et al. 2001; Jaward et al. 2004) have been coupled in a 0D (i.e. zero- dimensional), spatially resolved, box model. A 0D model means, for example, that the vertical variation of the fluxes is not accounted for. A box model means that the system has been subdivided into well-mixed and interconnected compartments. The model was applied using monthly means of satellite data and assuming that measured atmospheric concentrations are constant in time.

Satellite-based environmental data correspond to monthly climatological means (average 2001 – 2003) of *Level 3* data with global coverage and resolutions of 1°x1° or 0.5°x0.5°, presented in greater detail below. Level 3 refers to data that is designed for the end user, which has been calibrated with *in situ* observations and data assimilation techniques.

3.2 Satellite Data Used

3.2.1 Wind speed distributions at 10m above the surface of the sea

The surface wind speed was used in this study (u_{10}, m s^{-1}). Values were obtained from the NOAA Special Sensor Microwave/Imager (SSM/I) at a resolution of 1°x1° and an accuracy of ± 2 m s^{-1} (`http://lwf.ncdc.noaa.gov/oa/satellite/ssmi/ssmiwind.html`).

3.2.2 Aerosol parameters over the oceans

Aerosol values at a resolution of 1°x1° were obtained from the Moderate-Resolution Imaging Spectrometer Instrument (MODIS, `http://modis.gsfc.nasa.gov/`) on board the Terra satellite, part of NASA's Earth Observing System (EOS). In particular, we used the effective radius (r_{eff}, μm) and its standard deviation (which provides information about the size distribution of aerosols), the aerosol optical depth (AOD) and its standard deviation (related to the aerosol density in the atmosphere), and the fraction of optical depth corresponding to submicron aerosols (η, [0 1]). The approximate accuracy is $\pm$ 0.1μm for r_{eff}, $\pm$0.03*AOD (or $\pm$0.05*AOD in dust regimes), and 25% for η. MODIS aerosol retrieved measurements refer to values integrated over the air column and they refer to the size range detected by the instrument (aerosol diameters from 0.1 to 20 μm). This information is important to derive aerosol dry deposition velocities from satellite data (Jurado et al. 2004).

It should be pointed that deriving aerosol sizes or concentrations from remote sensing measurements has a higher uncertainty than other variables such as wind speed, SST and p_0 used in this study. Until recently, MODIS was the only sensor that gave information about aerosol sizes. This area of research is currently undergoing rapid development, and several satellite-based light imaging radars (lidars) are being launched (e.g. CALIPSO from NASA), providing information about the vertical structure of aerosol plumes, which is not available from MODIS data.

3.2.3 Precipitation data

Values of monthly rainfall rates (p_0, [mm month^{-1}]) and the fractional occurrence of precipitation (f, [0-1]) were obtained from SSM/I NOAA at a resolution of 1°x1° (`http://www.ncdc.noaa.gov/oa/satellite/ssmi/ssmiprecip.html`). Determination of rainfall by passive microwave sensors, such as SSM/I, may be underestimated during low rainfall periods and overestimated during wet periods, leading to some inaccuracies in the tropics. However, rainfall retrieval over the ocean from SSM/I represents the best compromise between estimation accuracy and spatial data coverage. Uncertainty is about 15 to 30% when compared to rain gauge data sets.

A novelty of the use of precipitation data in wet deposition modelling of POPs has been the consideration of the influence of the frequency of rain (f). Hence, the instantaneous flux of contaminants scavenged by rain may be quite substantial in a month with a low frequency of rain. The methodology developed is further described in Jurado et al. (2005).

3.2.4 Sea Surface Temperature (SST, [K])

Values were obtained from the Along Track Scanning Radiometer (ATSR) on board the European Space Agency ERS-2 satellite (`http://www.atsr.rl.ac.uk/`). SST images consist of monthly averaged data with a resolution of 0.5°x0.5° and an accuracy of ±0.3K.

3.2.5 Chlorophyll-*a* concentration (chl-*a*, mg m^{-3})

This was estimated from reflectance signals obtained from NASA's Sea-Viewing Wide Field-of-view Sensor (SeaWiFS) (`http://www.csc.noaa.gov/crs/rs_apps/sensors/seawifs.htm`). The resolution is 1°x1° and accuracies are around the 15%. This data allows the estimation of the phytoplankton biomass distribution in the surface mixed layer.

3.3 Demonstration Section

In this section we present the values of dry deposition flux, latitudinally-averaged for the Atlantic, together with satellite global maps of data that have a potential effect in the magnitude of the flux. Visually-based interrelations between this flux and that pertaining to the satellite data are explained, so that one can acquire the skills required to use the satellite images to understand better the latitudinally-averaged fluxes of POPs.

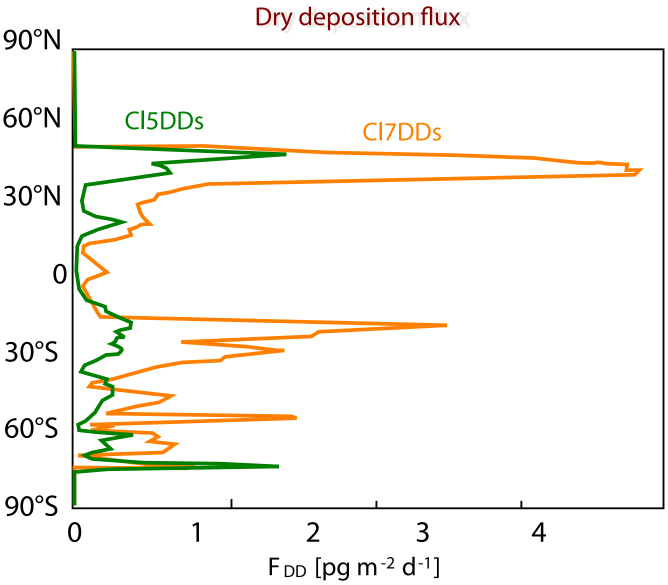

Figure 3.2 Averaged latitudinal profile of the dry aerosol deposition fluxes for Cl5DDs and Cl7DDs over the Atlantic Ocean, for the period October-December 1998.

As a reminder, the dry aerosol deposition flux is the deposition of aerosol-bound contaminants in the absence of rain. Figure 3.2 depicts an example of a latitudinally-averaged profile of dry deposition flux over the Atlantic for two reference compounds, the penta-dibenzo-p-dioxin (Cl5DDs) and the hepta-dibenzo-p-dioxin (Cl7DDs). The flux has been estimated using the methodology presented in the previous section, but developed in detail in Jurado et al. (2004). An example of measured air concentration data is depicted in Figure 3.3.

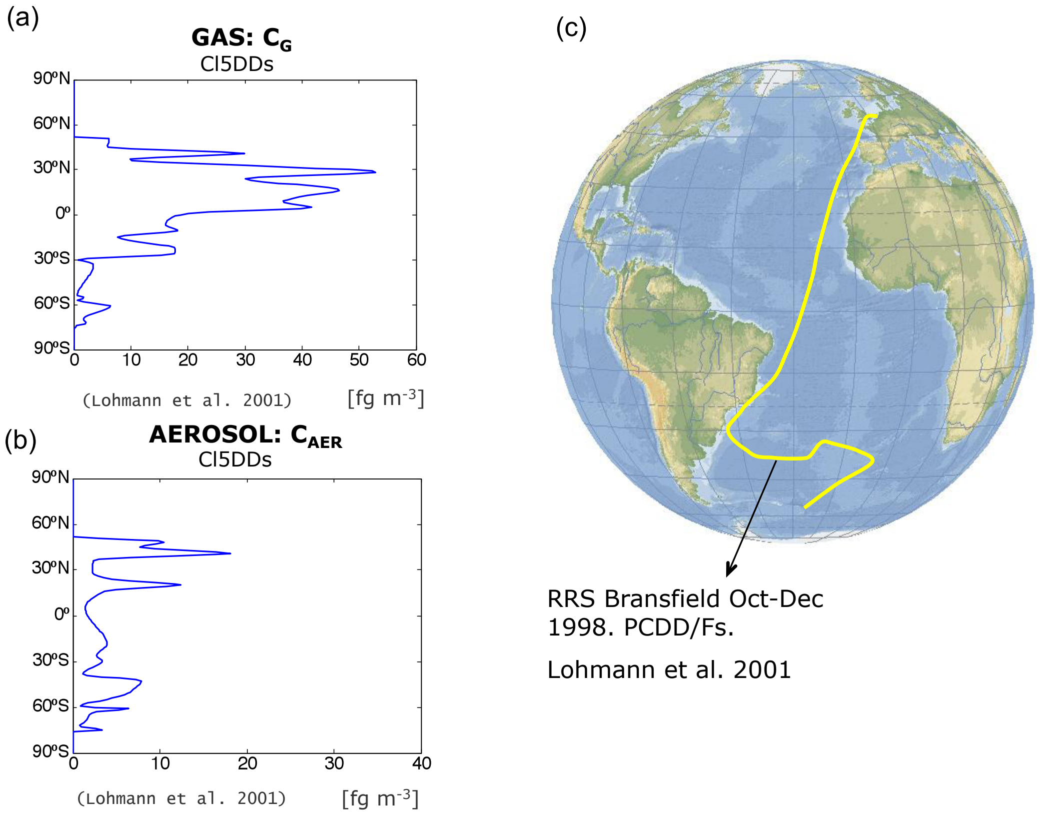

(Lohmann et al. 2001)

(Lohmann et al. 2001)

RRS Bransfield Oct-Dec 1998. PCDD/Fs.

Lohmann et al. 2001

Figure 3.3 Latitudinal profiles of Cl5DDs measured during a north-south Atlantic cruise: (a) gas and (b) aerosol sorbed profiles. Figure (c) depicts the cruise track.

For the interpretation of Figure 3.2 we provide the following satellite images: sea surface temperature (SST) (Figure 3.4), indicative of the temperature of the air close to the water surface, the effective radius (r_{eff}) (Figure 3.5), defined as the weighted integral of the volume-surface ratio and indicative of the size of the aerosol, the aerosol mass concentration derived from the aerosol optical depth (Figure 3.6) (Gasso and Hegg 2003), and the wind speed at a height of 10 m (u_{10}) (Figure 3.7).

As a first step to better understand the way that the dry aerosol deposition fluxes are connected to the environmental data provided in Figures 3.4 to 3.7, it is important to take into account the exact parameterization of this flux:

$$F_{DD} = V_D C_{AER} \tag{3.4}$$

where F_{DD} [ng m^{-2} s^{-1}] is the dry aerosol deposition flux, v_D [m s^{-1}] denotes the aerosol overall dry deposition velocity and C_{AER} [ng m^{-3}] is the POP aerosol-phase

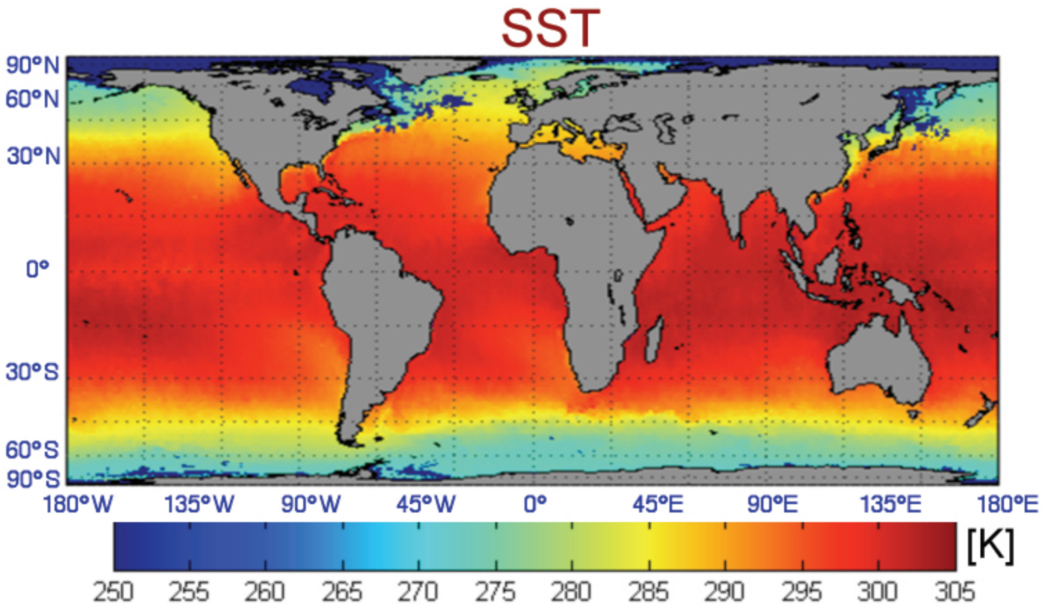

Figure 3.4 Global distribution of Sea Surface Temperature (SST) in January (climatological monthly mean of 1998 – 2000).

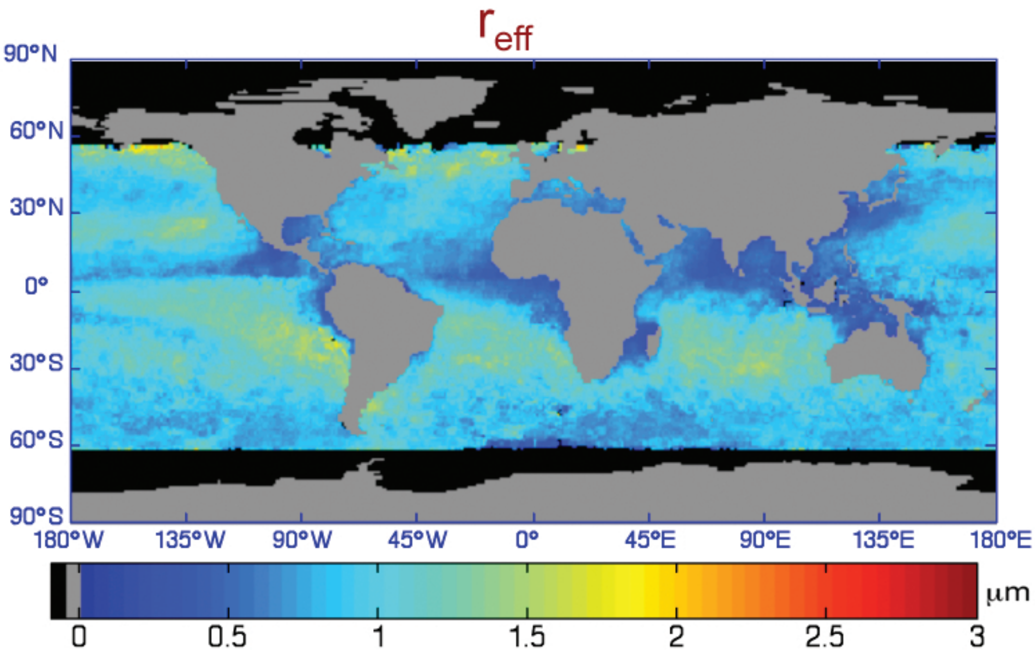

Figure 3.5 Global distribution of effective radius (r_{eff}) over the oceans in November (climatological monthly mean of 1998 – 2000).

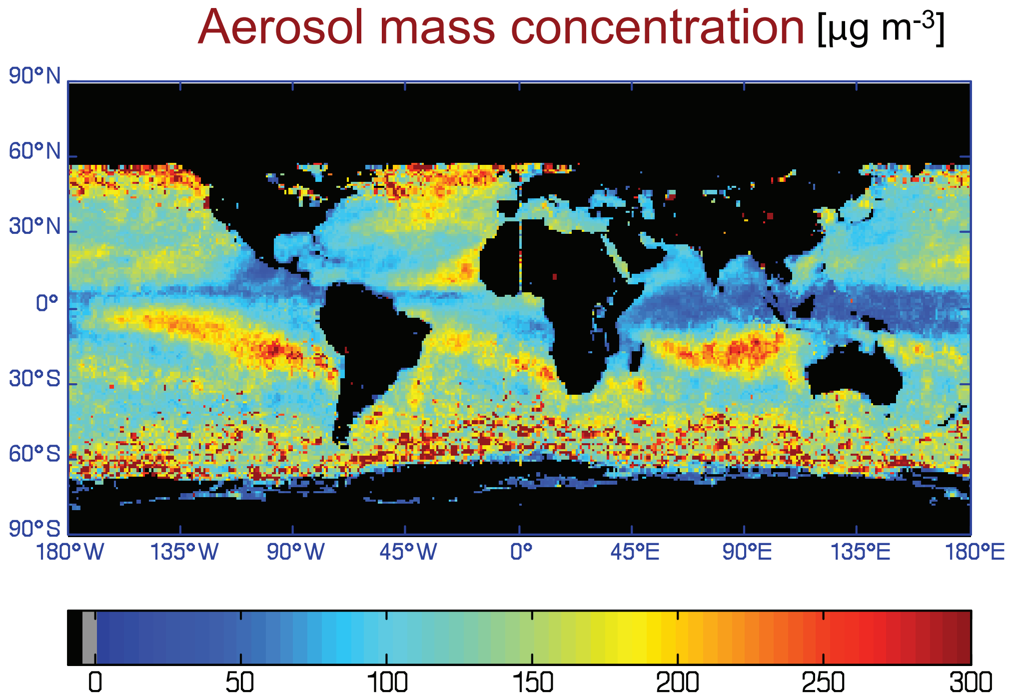

Figure 3.6 Global distribution of the aerosol mass concentration over the oceans in November (climatological monthly mean of 1998 – 2000). Derived from MODIS Aerosol Optical depth parameter, and the algorithm developed in Gasso and Hegg (2003).

concentration.

From Equation 3.4 one should note that the dry aerosol deposition flux is directly proportional to the POP-aerosol-phase. Indeed, major dry deposition fluxes will be found in regions with major amounts of contaminants in the aerosol phase. The tendency to be in the aerosol-phase instead of the gas-phase is highly dependent on the air temperature, so that a lower air temperature will cause a higher partition to the aerosol phase. A map of SST , representative of the temperature of the air above the ocean surface, provides information of the regions over the oceans with a higher proportion of contaminants in the aerosol phase i.e. the temperate regions at higher latitudes.

The sea surface temperature (Figure 3.4) cannot be the only variable affecting the latitudinal trend in the fluxes from Figure 3.2, because it follows a smooth increase towards higher latitudes, while the fluxes depict an important variability. Other environmental variables, with a higher patchiness, should affect the magnitude of the fluxes. We envisage that the effective radius (Figure 3.5), aerosol mass concentration (Figure 3.6) or the wind speed (Figure 3.7) could contribute because their global distribution presents a higher variability than the SST.

How do Figures 3.5 to 3.7 combine to explain the fluxes in dry deposition of

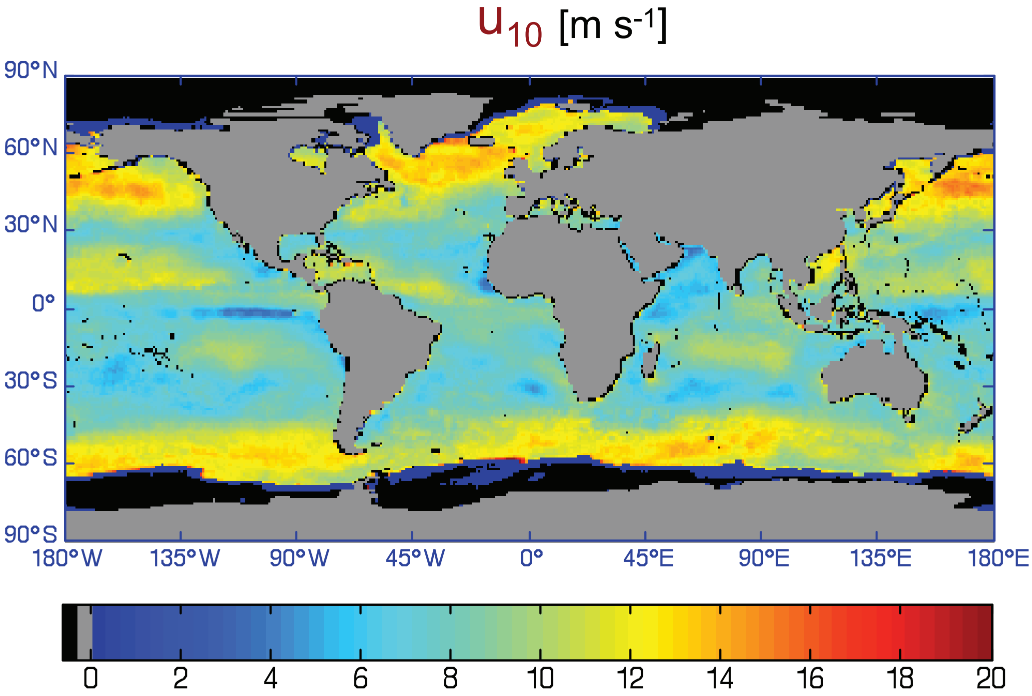

Figure 3.7 Global distribution of the wind speed (u_{10}) over the oceans in November (climatological monthly mean of 1998 – 2000).

POPs? The answer is found in the next variable, not yet assessed in equation 3.4, the overall dry deposition flux v_D. The v_D is greatly influenced by the aerosol size, by the atmospheric turbulent diffusion and by the atmospheric growth of particles at a high humidity. In particular, v_D will increase with the particle diameter and the wind speed for diameters >0.1 μm, governed by gravitational settling. Also, a high concentration of aerosol in the atmosphere will increase the dry deposition velocity. Knowing this information, it is possible to relate the large increase in the fluxes around 15°S to an increase of the effective radius, indicative of the size of aerosol particles, or the aerosol mass concentration in the Atlantic around this latitude. Furthermore, we can relate the peaks in the dry deposition fluxes around 60°S to strong winds in the Southern Ocean.

We end this section by explaining the differences in the fluxes of the two depicted contaminants: Cl5DDs and Cl7DDs. This is an example of how physico-chemical properties of the chemical compounds affect the fluxes. We see that the relative increase of dry deposition fluxes of the Cl7DFs in higher latitudes is greater than for Cl5DFs. This is because Cl7DFs sorb stronger to the organic matter of the aerosol, causing a major relative presence of those compounds in the aerosol phase. As a general rule, compounds with higher molecular weight will have less solubility in water, a higher affinity to organic matter and a lower vapour pressure.

3.4 Training and Questions

Q 1: Do you see any links between the flux of wet deposition (Figure 3.8), latitudinally-averaged for the Atlantic, and the satellite retrieved precipitation rate (Figure 3.9), referred to for the same climatological month of November? How are the data of sea surface temperature (Figure 3.4) useful to determine the wet deposition flux?

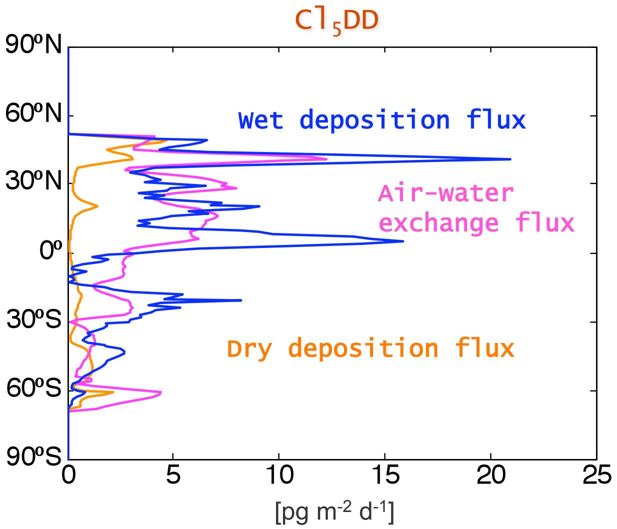

Figure 3.8 Averaged latitudinal profiles of the atmospheric depositional fluxes for the Atlantic Ocean for Cl5DDs.

To answer this question it is important to take into account the parameterization of the wet deposition flux. The removal of semivolatile compounds by rain results from the scavenging both of gaseous dissolved compounds and particle-bound compounds. A common assumption is that the total wet deposition flux (F_{WD} [ng m^{-2} s^{-1}]) is the product of the total (dissolved and particulate) concentration of contaminants in the rain (C_R [ng m^{-3}]) and the precipitation rate (p_0 [m s^{-1}]). Furthermore, since C_R is generally unknown, it is commonly expressed in terms of the concentration of contaminant in the aerosol (C_{AER} [ng m^{-3}]) and the gaseous phases (C_G [ng m^{-3}]):

$$\begin{aligned} F_{WD} &= p_0 C_R = F_{WD\_Gaseous} + F_{WD\_Particulate} \\ F_{WD\_Gaseous} &\cong \frac{C_G p_0 H}{RT} \\ F_{WD\_Particulate} &\cong C_{AER} p_0 2.10^5 \end{aligned} \tag{3.5}$$

where R is the ideal gas constant equal to 8.13 Pa m^3/K mol, and H is the Henry's law constant [Pa m^3/mol], defined as the ratio between the compound's saturated liquid vapour pressure and its solubility in water, and dependent on physicochemical properties and environmental data.

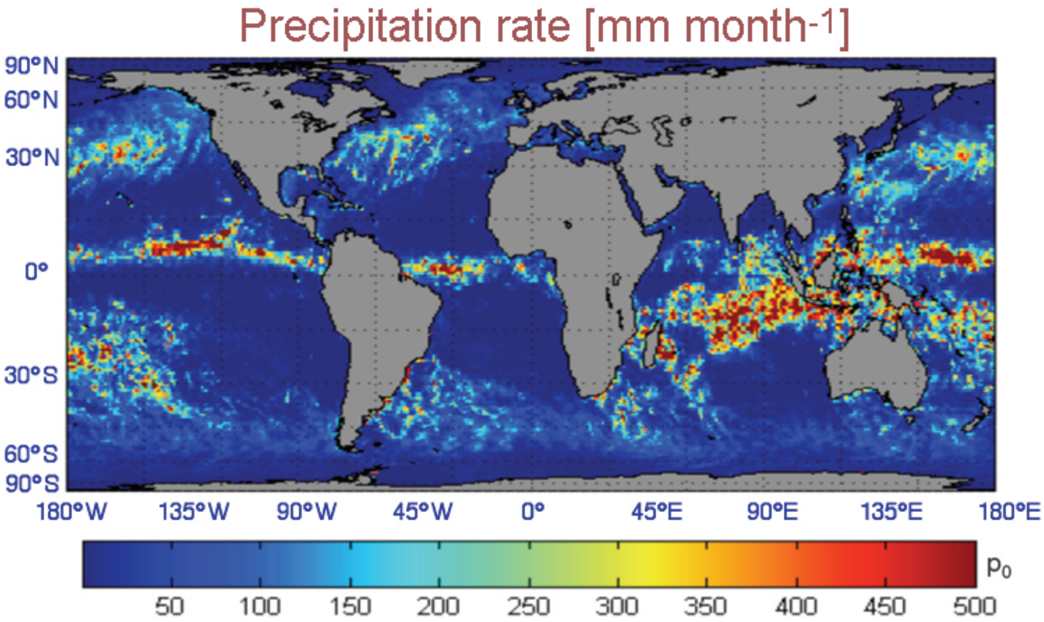

Figure 3.9 Global distribution of the precipitation rate (p_0) over the oceans in November (climatological monthly mean of 1998 – 2000).

Q 2: Which are the main satellite images, already displayed in this case-study, that potentially affect the flux of air-water exchange? Also consider the global distribution of chlorophyll-*a* depicted in Figure 3.10.

Again, to answer this question, it is important to first examine the parameterization of this flux. The flux of gaseous contaminants between the atmosphere and the oceans is driven by a concentration difference and by the transport due to molecular and turbulent motion. This flux combines turbulent and molecular diffusion since it occurs through an interface, thus the parameterization is not straightforward. It is based in the classical two-layer stagnant boundary layer model, where it is assumed that a well-mixed atmosphere and a well-mixed surface ocean are separated by a stagnant film through which gas transport is controlled by molecular diffusion. The resulting net air-water exchange flux (F_{AW} [ng m^{-2} s^{-1}]) is a function of a term with velocity units (the air-water mass transfer coefficient k_{AW}, [m s^{-1}]), the POP dissolved concentration in the water (C_W^{dis} [ng m^{-3}]) and the corresponding concentration in the gaseous phase in equilibrium (C_G RT/H). This flux is, in fact, the net difference of two processes acting in parallel: absorption of gaseous POPs from the atmosphere to the water (F_{AW_abs}) and the volatilization of POPs from the water to the atmosphere (F_{AW_vol}).

$$F_{AW} = F_{AW\_abs} - F_{AW\_vol} = k_{AW}\left(\frac{C_G RT}{H} - C_W^{dis}\right) \tag{3.6}$$

where H is, again, the Henry's law constant and k_{AW} the air-water mass transfer

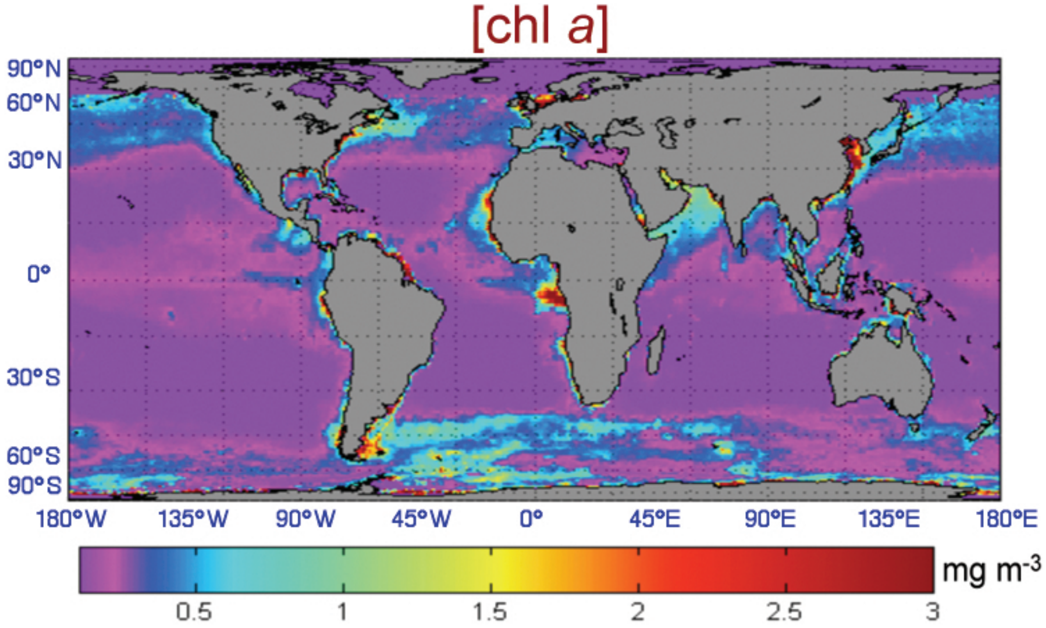

Figure 3.10 Global distribution of the concentration of chlorophyll-*a* (chl-*a*) in the oceans in January (climatological monthly mean of 1998 – 2000).

coefficient. k_{AW} describes the rate at which chemicals partition between air and water surface and comprises resistance to mass transfer in both water (k_W [m s^{-1}]) and air films (k_A [m s^{-1}]):

$$\frac{1}{k_{AW}} = \frac{1}{k_W} + \frac{RT}{k_A H} \tag{3.7}$$

These mass transfer coefficients have been empirically defined based upon field studies using tracers such as CO_2, SF_6 and O_2. k_W is calculated from the mass transfer coefficient of CO_2 in the water side (k_W,CO_2 [m d^{-1}]), itself generally correlated solely to wind speed (u_{10}, [m s^{-1}]):

$$k_W = k_{W,CO2} \left(\frac{Sc_{POP}}{600}\right)^{-0.5} \tag{3.8}$$

$$k_{W,CO2} = 0.24u_{10}^2 + 0.061u_{10}^2 \tag{3.9}$$

where Sc_{POP} [dimensionless] is the Schmidt number of the POP and 600 is the Schmidt number of CO_2 at 298K. Similarly k_A can be estimated from the mass transfer coefficient of H_2O in the air side (k_A,H_2O [m d^{-1}]), also generally parameterized as a function of the wind speed:

$$k_A = k_{A,H20} \left(\frac{D_{POP,a}}{D_{H20,a}}\right)^{0.61} \tag{3.10}$$

$$k_{A,H20} = 0.2u_{10} + 0.3 \tag{3.11}$$

where $D_{POP,a}$ and $D_{H2O,a}$ [$cm^2\ s^{-1}$] are the diffusivity coefficients of the POP and H_2O in air respectively.

Q 3: How can we determine the effect of short-term variations of the environmental data in the air-water POP fluxes if we use monthly means from satellite data?

3.5 Answers

A 1: Yes, we observe links between Figure 3.8 and Figure 3.9. In Figure 3.8 we observe an important variability in the Atlantic profiles of the fluxes, especially noteworthy for the wet deposition fluxes. Since the flux of wet deposition is directly proportional to the precipitation rate (see Equation 3.7), we can relate this variability to the spatial variability of the precipitation rates depicted in Figure 3.9. Therefore, it is clearly important to consider spatially-resolved data for the global assessment of POP cycling; in this context the use of remote sensing data is greatly justified. On the other hand, the wet deposition flux peaks in the high precipitation rates areas, such as in the Intertropical Convergence Zone (ITCZ). The positive gradient towards the northern hemisphere is related to the major emissions in the northern hemisphere.

As already pointed out in the Demonstration section, the SST data will be useful to assess which fraction of contaminants partition to the gaseous phase and which fraction of the contaminants partition to the aerosol phase. By looking in detail at Equation 3.7 we see that the fraction of contaminants that are in the gaseous phase versus the ones in the aerosol phase relates to the relative importance of the wet-gaseous flux versus the wet-particle flux. The temperature will affect also the gaseous wet deposition flux through its effect in H and also in the denominator of Equation 3.7. Putting it all together, the regions with lower SST, i.e. polar regions, will favour the particle-wet deposition.

A 2: The satellite-based remote sensing data that affect air-water exchange fluxes are sea surface temperature (Figure 3.4), wind speed (Figure 3.7) and chlorophyll-*a* (Figure 3.10). From Equations 3.6, 3.9 and 3.11, it is clear that wind exerts an important effect on k_{AW}. On the other hand, temperature influences significantly the magnitude of k_{AW}through its influence on diffusivities, Schmidt numbers and H. Temperature may affect the partition between aerosol and gaseous phases in the atmosphere and between dissolved and particulate phases in the water. On the other hand, since it has been proven that the particulate phase to which pollutants sorb is mainly phytoplankton, it can be foreseen that the amount of phytoplankton in the water column will modify the air-water exchange flux. This amount of phytoplankton is estimated from the satellite-derived chlorophyll-*a* concentration.

A 3: It is important to account for the short-term variability of wind speed and precipitation in the depositional fluxes of POPs because it can potentially affect the monthly averages. Averages have been corrected by the appropriate parameter. If an oceanic Weibull distribution of wind speed is considered, then a shape parameter of 2 seems appropriate. Conversely, precipitation amounts can be modelled by an exponential distribution that depends on the average non-zero precipitation amount. More information can be found in Dachs et al. (2002) and Jurado et al. (2005).

3.6 References

Dachs J, Lohmann R, Ockenden WA, Méjanelle L, Eisenreich SJ, Jones KC (2002) Oceanic biogeochemical controls on global dynamics of Persistent Organic Pollutants. Environ Sci Technol 36 (20): 4229-4237

Gassó S and Hegg DA (2003) On the retrieval of columnar aerosol mass and CCN concentration by MODIS. J Geophys Res 108(D1): 4010, doi:10.1029/2002JD002382.

Jaward FM, Barber JL, Booij K, Dachs J, Lohmann R and Jones KC (2004) Evidence for dynamic air-water coupling and cycling of persistent organic pollutants over the open Atlantic Ocean. Environ Sci Technol 38 (9): 2617-2625.

Jurado E, Jaward F, Lohmann R, Jones KC, Simó R, Dachs J (2004) Amospheric dry deposition of persistent organic pollutants to the Atlantic ocean and inferences for the global oceans. Environ Sci Technol 38 (21): 5505-5513.

Jurado E, Jaward F, Lohmann R, Jones KC,Simó R, Dachs J (2005) Wet deposition of Persistent Organic Pollutants to the global oceans. Environ Sci Technol. 39 (8): 2426-2435.

Jurado, E., Dachs, J., Duarte, C. M., Simó, R (2008) Atmospheric deposition of Organic and Black Carbon to the global oceans. Atmos Environ 42: 7931-7939.

Lohmann R, Ockenden WA, Shears J and Jones KC (2001) Atmospheric distribution of polychlorinated Dibenzo-p-dioxins, Dibenzofurans (PCDD/Fs), and Non-Ortho Biphenyls (PCBs) along a North-South transect. Environ Sci Technol 35 (20): 4046-4053.

Simó R, Dachs J (2002) Global ocean emission of dimethylsulfide predicted from biogeophysical data. Global Biogeochem Cy 16 (4): 26-1 26-9

3.6.1 Further reading

Jurado E (2006) Modelling the ocean-atmosphere exchanges of Persistent Organic Pollutants. PhD-thesis `http://www.tesisenxarxa.net/TDX-0330107-123245/index.html`

Mackay D (2001) Multimedia Environmental Models. The fugacity approach. Lewis Publishers, Florida

Case Study 4

Impacts of European Atmospheric Air Pollution on Water Nutrients in the Atlantic Ocean, Baltic Sea, and Mediterranean Sea

Ana I. Prados*[1] **and James Acker**[2]

4.1 Background Information

Combustion activities worldwide lead to atmospheric Nitrogen Oxides (NO_x) emissions which can be transported over long distances and, via dry and wet deposition, contribute to excess nutrient loads in the world's rivers, estuaries and oceans, leading to water pollution and impacts such as the commonly observed coastal algal blooms. Satellite imagery can be used to track these anthropogenic NO_x emissions and to study their potential impacts on water quality. This chapter provides a guide for obtaining and analyzing nitrogen dioxide imagery from the Ozone Monitoring Instrument (OMI).

The production of carbon, or primary productivity, by photosynthetic marine organisms provides the energy which ascends the marine trophic level ladder, from zooplankton to fish to whales, providing sustenance to the marine benthos when phytoplankton detritus descends to the seafloor. Phytoplankton productivity is controlled by the location and movement of these free-floating plants in oceanic currents, but their growth rate is determined primarily by the availability of sunlight and the necessary concentrations of vital nutrients. Enhanced phytoplankton productivity due to nutrient excess in waterways can lead to eutrophication, where organic detritus on the sea floor causes low dissolved oxygen, or zero dissolved oxygen concentrations in bottom waters due to bacterial decomposition. Increased nutrient levels may also cause species shifts from the common phytoplankton species to less desirable phytoplankton species, including species that are noxious or hazardous due to toxicity, otherwise known as harmful algal blooms.

The two primary marine macro-nutrients are familiar to many gardeners and

---

[1] University of Maryland Baltimore County, Joint Center for Earth Systems Technology, Greenbelt, Maryland, USA. **Email address:* `aprados@umbc.edu`

[2] Goddard Earth Sciences Data and Information Services Center, Wyle IS LLC, Greenbelt, Maryland, USA

grounds keepers as the basic elements of fertilizer: nitrate and phosphate. Macronutrients can enter water ways either via terrestrial sources or via direct or indirect atmospheric deposition. Terrestrial sources of nutrients can be divided into two categories: point and non-point sources. The main terrestrial non-point sources of nutrients are fertilizers from the agricultural sector and runoff from impervious surfaces. In some regions of the world, the agricultural sector contributes the largest fraction of the entire nitrogen load. Nitrate and phosphate are also produced a result of various industrial processes and they are present in household chemicals such as dishwasher and laundry detergents. These pollutants are discharged into water ways via municipal water systems and they comprise the major point sources of nitrogen pollution. Although nitrogen and phosphate discharges from municipal waste water treatment plants today have been greatly reduced in some countries, nutrients continue to contribute to water pollution in rivers, estuaries and oceans worldwide.

In estuaries, nutrients are delivered by fresh water flow from rivers and streams into bays and sounds; where river flows enter the ocean directly, the nutrients from river waters can be transported hundreds of miles and foster enhanced productivity in their region of influence. Two fundamental processes, upwelling and mixing, bring deep-water nutrients to the surface, where they foster phytoplankton growth, such as the noteworthy Peru and Benguela upwelling zones. Because phytoplankton requires about 16 times as much nitrate as phosphate for optimum growth, nitrate is frequently the ‘limiting nutrient’, meaning that it controls the level of phytoplankton growth in ocean waters. Although nitrates are more commonly the limiting nutrient, there are times of the year and regions where it is possible for phosphate, iron, or silica to be the limiting nutrient.

Another important source of nitrogen to ocean waters is direct atmospheric deposition of nitrogen species. Atmospheric nitrogen species also contribute to nutrient loads in ocean waters through indirect deposition when nitrogen species deposit onto rivers that then feed into estuaries and open oceans. Combustion processes such as energy production from coal, vehicular emissions from gasoline and diesel fuel, other industrial activities, and fires lead to the emission of nitrogen oxide pollutants. Using the air shed for the Long Island Sound watershed as an example, the largest sources of nitrogen emissions are transportation NO_x (39%), electric utility NO_x (26%) and ammonia emitted from animal waste (16%). These nitrogen oxide species can undergo chemical modifications in the gas phase or liquid phase to species such as nitric acid and aerosol particles. When atmospheric nitrogen species are deposited on rivers, estuaries, or in the open ocean, they can also induce both surface water acidification and nitrification or excess nitrate. Sulfuric acid, which also has anthropogenic sources, is another contributor to water acidification. The deposited nitric acid is converted in surface seawater, which is basic (pH approximately 8.1 – 8.4), to nitrate, becoming biologically available.

Over certain water bodies around the world, atmospheric nitrogen deposition constitutes a large fraction of the total nitrogen load, such as open ocean areas close to large sources of air pollution, regions with little water upwelling, and regions with little influence from terrestrial sources of nutrients. This atmospheric contribution of nitrogen augments primary productivity, particularly in oligotrophic waters. According to Pryor and Sørensen (2002), dry deposition of nitric acid, nitric oxides, particulate nitrate, and ammonia comprises about 20 – 40% of the total nitrogen flux in oceanic study regions. Prospero et al. (1996) reported that anthropogenic nitrogen emissions cause the deposition rate of nitrogen oxide species "NO_y"to the North Atlantic Ocean to be about five times greater than pre-industrial levels; this increase is similar for reduced nitrogen species ("NH_x"). Prados et al. (1999) found that much of the NO_y in the North Atlantic is transported over long distances. Jickells (1998) wrote that approximately one-third of anthropogenic nitrogen emissions in the North Sea are comprised of nitrogen dioxides; this percentage is similar for the Kattegat in the Baltic Sea, but in the form of reduced nitrogen. For estuaries such as the Chesapeake Bay in the United States, with substantial terrestrial inputs of nitrogen, the importance of atmospheric nitrogen deposition is reduced compared to riverine input, but is still substantial. He also notes that airborne sea salt from sea spray contributes to the formation of large aerosol particles laden with nitrate, which increases the efficiency of atmospheric nitrate deposition substantially. According to Duce et al. (2008) atmospheric nitrogen deposition could account for up to 3% of new annual oceanic primary productivity, an increase that is 10 times larger than pre-industrial times, and this represents about one-third of the primary productivity caused by all external (water and air) nitrogen input to the oceans.

Atmospheric nitrogen deposition can also influence the oceanic release of nitrous oxide (N_2O), a greenhouse gas. According to Duce et al. (2008), "... the increase in AAN [anthropogenic atmospheric fixed nitrogen] has led to nearly an order of magnitude increase in anthropogenic N_2O emission from the oceans." Finally, atmospheric nitrogen deposition can shift the nitrogen/phosphate balance in surface waters. One of these areas is the North Atlantic Ocean, where Fanning (1989) documented, based on GEOSECS data, that while phosphate concentrations were depleted, nitrate and nitrite were detectable. He postulated that this was due to air pollution from the Eastern Seaboard, citing Levy and Moxim's (1989) map of global atmospheric combustion-produced nitrogen. In this area, phytoplankton productivity would have otherwise used up the available phosphate but atmospheric nitrogen provided an excess of nitrate, making phosphate the limiting nutrient.

This investigation uses atmospheric NO_2 satellite observations from the Ozone Monitoring Instrument (OMI) to examine its potential effect on water quality in the Atlantic Ocean, Mediterranean Sea, and Baltic Sea. The OMI NO_2 algorithm retrieval has been described by Bucsela et al. (2006). The product to be demonstrated is the total tropospheric column density in molecules/cm^2. This represents the integrated NO_2 amount from the surface of the earth to the tropopause (the atmospheric boundary between the troposphere and the stratosphere). Because OMI NO_2 is a

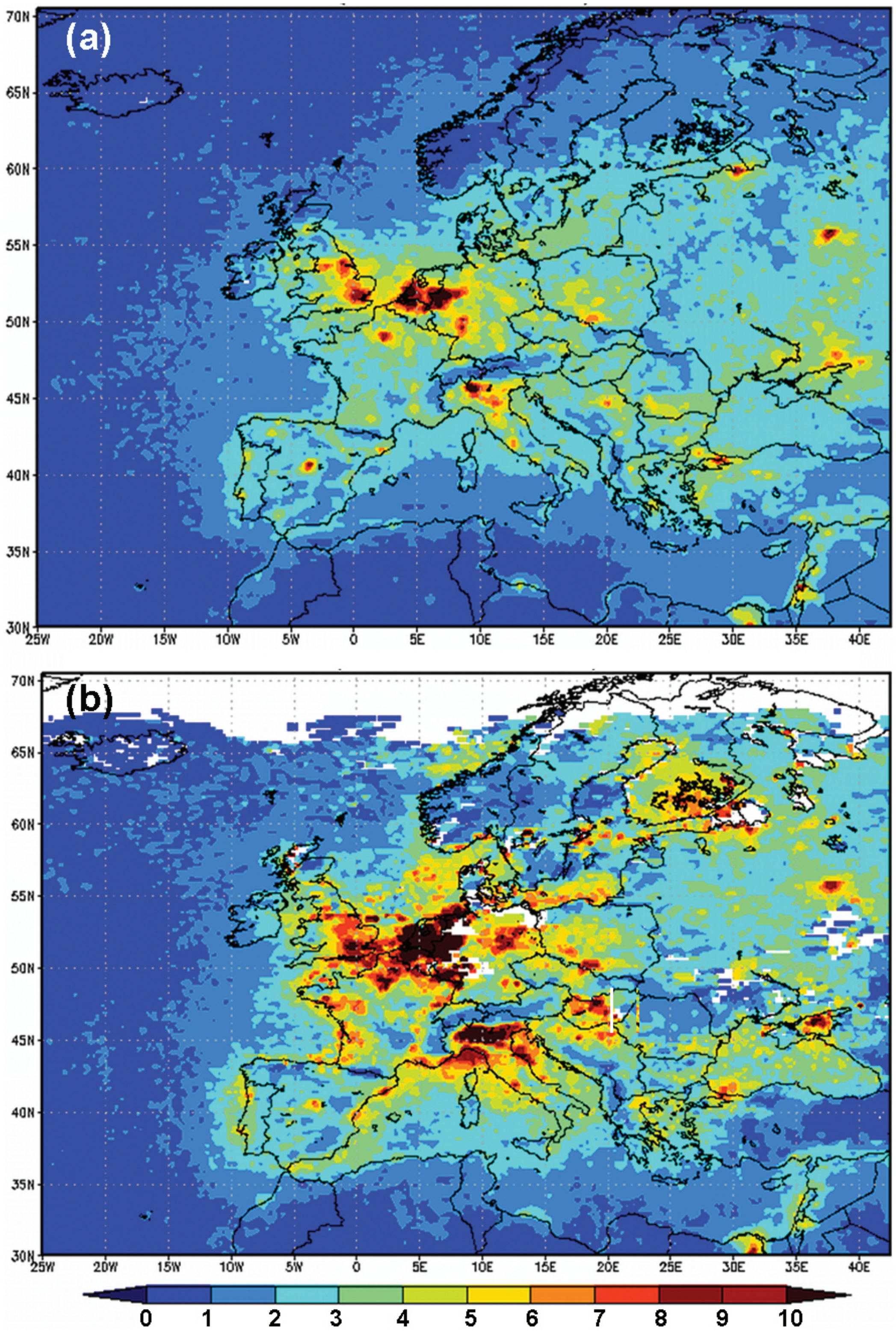

Figure 4.1 Giovanni mean monthly OMI (Ozone Monitoring Instrument) tropospheric NO_2 column for (a) July 2008 and (b) January 2008.

column measurement, it does not give us information regarding its vertical distribution. NO_2 has a relatively short photochemical lifetime (from hour to days) and tends to concentrate near the surface of the earth. OMI NO_2 tropospheric column measurements have been shown to be sensitive to boundary layer, concentration based, comparisons with measurements from ground based networks (Celarier et al. 2008; Lamsal et al. 2008). However, atmospheric convective processes can also lead to high NO_2 concentrations in the mid to upper troposphere (Prados et al., 1999).

OMI NO_2 tropospheric columns from 2005 until present are available globally from several sources. The Royal Netherlands Meteorological Institute (KNMI) Tropospheric Emissions Monitoring Internet Service (`http://www.temis.nl/airpollution/no2col/no2regioomi_col3.php`) has the advantage of providing near real-time imagery and maps for specific regions of the world. Another method for obtaining OMI NO_2 data is from the NASA GES DISC Interactive Online Visualization ANd aNalysis Infrastructure (Giovanni). Giovanni is a decision-support tool for air quality applications (Prados et al., 2010), among others, and it has the advantage of providing analysis tools, in addition to visualization capabilities.

This chapter will demonstrate how to access and interpret gridded 0.25 x 0.25 degree OMI NO_2 tropospheric columns through Giovanni. Visualizations are available both as jpg images and as a KMZ files which can be uploaded through Google Earth. Giovanni allows users to select areas of interest through an interactive map for the generation of latitude/longitude daily maps or temporally averaged maps. There are also a number of image analysis tools such as time series and correlation plots and maps.

4.2 Demonstration

STEP 1: Go to the main Giovanni web page `http://giovanni.gsfc.nasa.gov`

STEP 2: Access Giovanni OMI NO_2

Go to the table in the main Giovanni page and click on 'Aura OMI L3' link.

STEP 3: Generate Maps of OMI NO_2

In this section, you will generate several latitude/longitude plots to help with your image analysis.

1. Spatial Selection: Click on the map and with the mouse select a box that includes Europe, the North Atlantic Ocean, the Baltic Ocean, and the Mediterranean Ocean. Alternatively, enter these latitudes and longitudes in the boxes below the maps: North: 70.5; South: 30; East: 42.5; West: -25
2. Parameter Selection - select the box with the following parameter: NO_2 Tropospheric Column (Cloud-Screened at 30%).
3. Temporal Selection: Begin Date = 2008, July 1; End Date = 2008, July 31

4. Under "Select Visualization," select "Lat-Lon Map, Time-Averaged" and then click on "Generate Visualization". It will take a few moments for Giovanni to create the plot. Your plot should look similar to the one shown in Figure 4.1a.
5. Repeat the above for the following Time period: January 1 – January 31, 2008. Your plot should look similar to the one in Figure 4.1b.

STEP 4: Visualize images on Google Earth and download of GIF images

1. From the results page for the January 2008 visualization you just created, click on the "Download Data" tab at the top of the page.
2. To download a KMZ or other data files click on the items on the last column.
3. To view the image on Google Earth, click on the KMZ icon, then upload to Google Earth directly or you can choose to save the file, then open Google Earth, and then open the file after you start Google Earth.
4. Zoom in the country of Spain and make a note of where the OMI NO_2 is the highest. Your plot should look similar to Figure 4.2, which shows the OMI NO_2 over Spain overlaid on Google Earth.
5. To download a gif image click on the file name at the bottom of the first column.

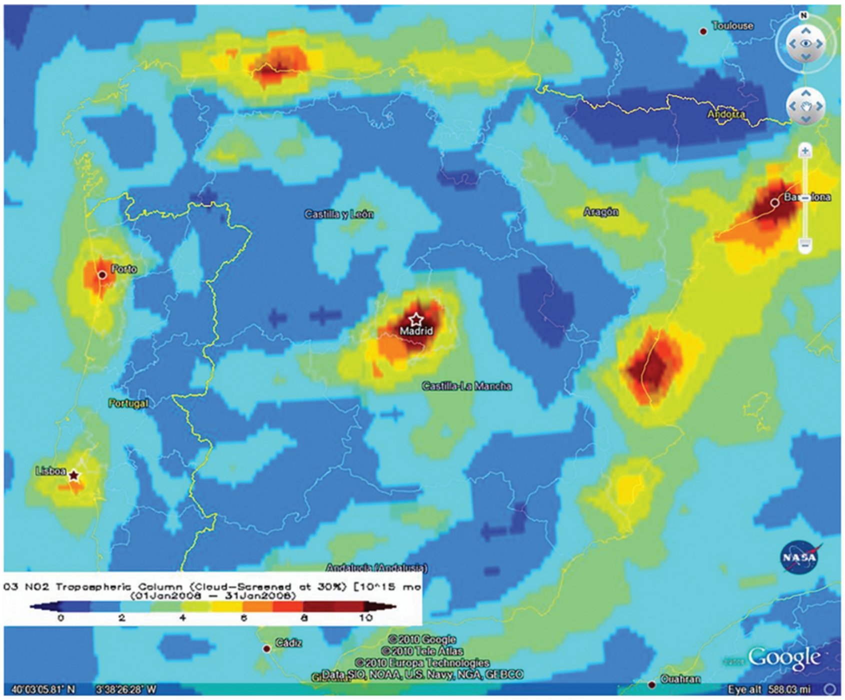

Figure 4.2 Giovanni mean monthly OMI tropospheric NO_2 column for July 2008 over Spain using a KMZ output data file from Giovanni on Google Earth.

STEP 5: Generate Animation Plots of NO_2

1. Now go back to the 'OMI AURA L3' page (click on Home in the tab above the

map).
2. Leave the same Spatial and Parameter Selections as in STEP 3
3. Temporal Selection: Begin Date = 2008, February 1 End Date = 2009, February 29
4. Under "Select Visualization," select "Animation" and then click on "Generate Visualization". You can use the tabs at the bottom of the plot to advance images one by one or to visualize all the images as an animation. We will be focusing on the images for February 12 – 14 (Figure 4.3).

STEP 6: Generate an OMI NO_2 Time Series Plot

1. Go back to the 'OMI AURA L3' Page (click on Home in the tab above the map).
2. Now we will want to narrow our frame to observe NO_2 over the North Sea between England and Norway. Select a region of the North Sea or alternatively, enter these latitudes and longitudes in the boxes below the maps: North: 59.6; South: 52.6; East: -84; West: -96 3.
3. Parameter Selection (select the box for the following parameter): NO_2 Tropospheric Column (Cloud-Screened at 30%).
4. Temporal Selection: Begin Date = 2008, Feb 1; End Date = 2008, Feb 29
5. Under “Select Visualization," select “Time Series" and then click on ‘Generate Visualization". It will take a moment for Giovanni to create the plot. If you chose the same latitudes and longitudes above, your plot should look similar to Figure 4.4. Write down the days in February in which OMI NO_2 is the highest over this region.

STEP 7: Image Interpretation

In order to interpret the images, look at the colour bar at the bottom of each map, which has a scale from 1 to 10 x 10^{15} molecules/cm^2. Values over 7 indicate moderately polluted conditions. Keep in mind that these are column measurements. We do not know whether the pollution is closer to the surface, where it can have greater impacts on human health, or higher in the atmosphere. OMI data, however, are not always available. One of the main reasons for lack of data is cloudiness. The OMI data available through Giovanni have been automatically screened (the region appears white in the map because the data are not available) when the cloud cover is 30% or greater. The last figure you created (Figure 4.4) is called a time-series, and it shows the averaged NO_2 tropospheric column (y-axis) over the regions (square) you selected in Giovanni for each day. The day of the month is shown in the x-axis.

4.3 Questions

Q 1: Look at the July 2008 map you generated (Figure 4.1a). Which countries have the highest NO_2 emissions and why? Think about what kinds of human activities in those countries may be contributing to the higher NO_2 levels compared to other

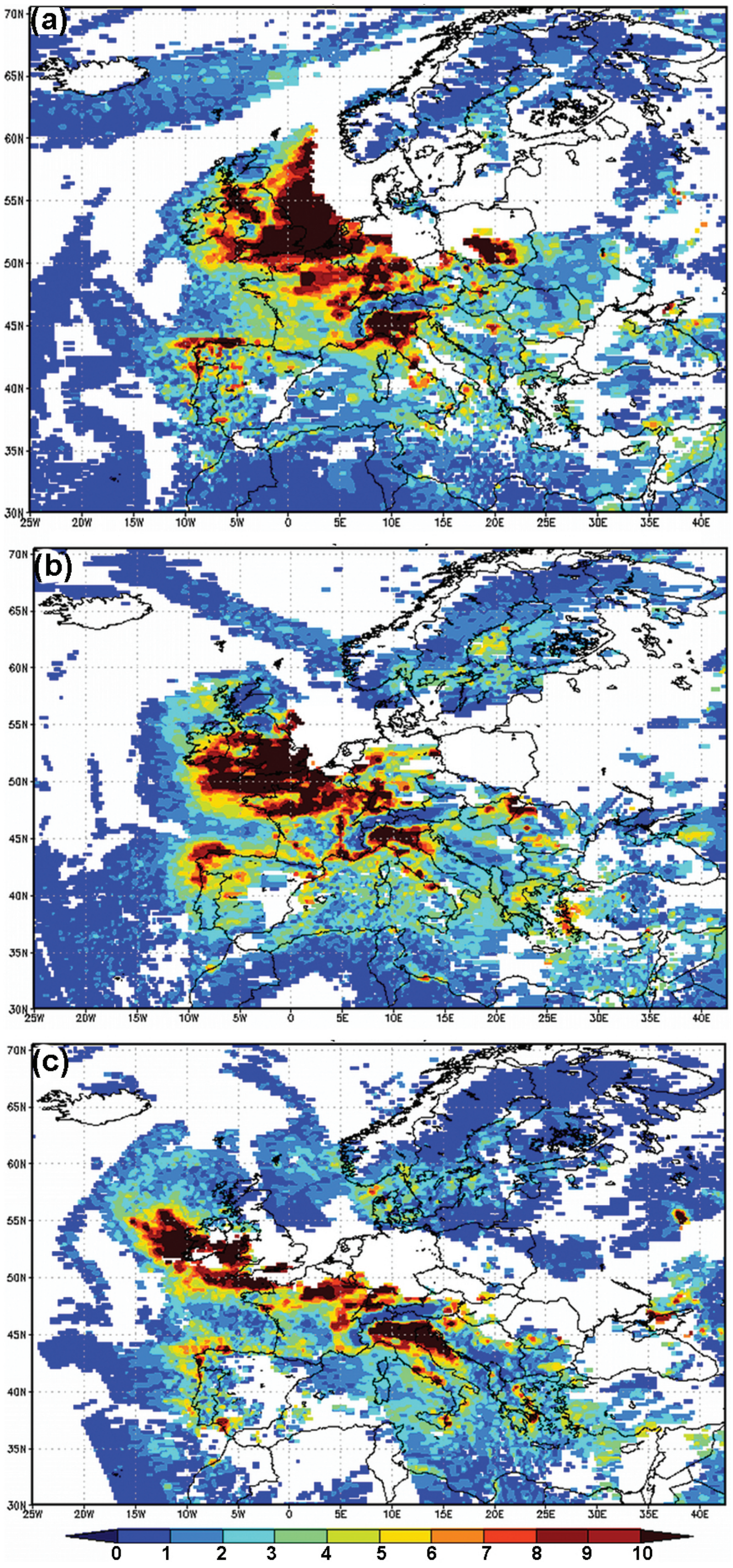

Figure 4.3 Giovanni daily OMI tropospheric NO_2 column on (a) 12 February 2008, (b) 13 February 2008 and (c) 14 February 2008.

countries.

Q 2: Look at the January 2008 map you generated (Figure 4.1b). How do the mean values in January compare to those in July? Explain why the NO_2 tropospheric column is over land is higher in one month than in the other.

Q 3: During which month (January or July) would one expect a greater amount of NO_2 atmospheric deposition over the Baltic Sea, Mediterranean Sea, and the Atlantic Ocean?

Q 4: Look at the NO_2 values in Spain on January, 2008 (Figure 4.2). Which parts of Spain have the highest NO_2 concentrations and why? List several locations and activities in those locations which could be contributing to those high NO_2 concentrations. Why are some parts of Spain more polluted than others?

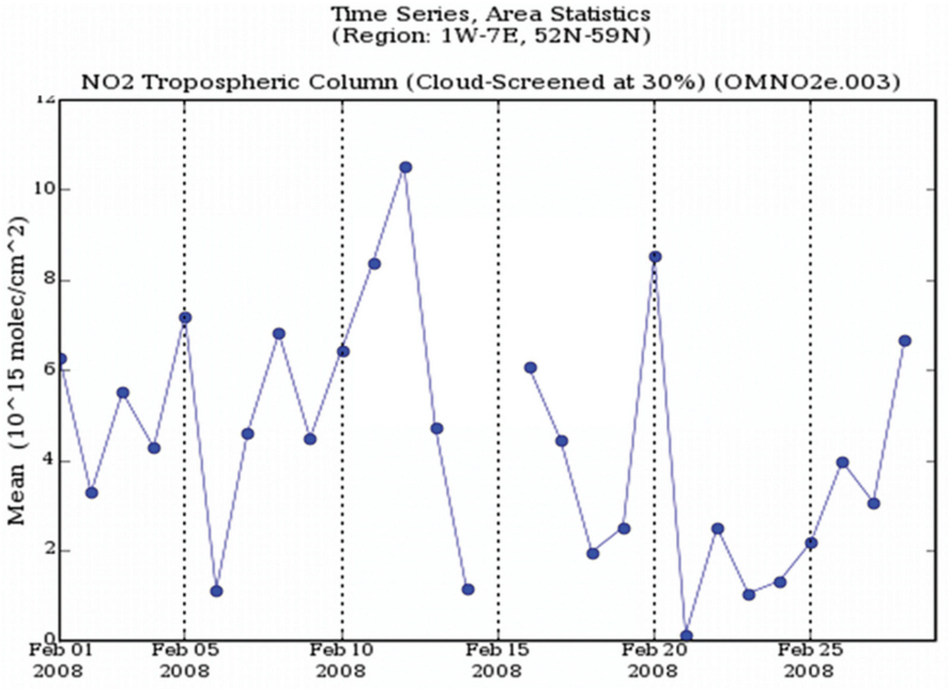

Figure 4.4 Giovanni time series of OMI tropospheric NO_2 column over the North Sea for February 2008.

Q 5: What are the main differences between land and the surrounding oceans in Figures 4.1a and b? Which coastal areas in Europe and surrounding oceans would we expect to have the greatest problems with ocean productivity and water pollution impacts such as algal blooms?

Q 6: Pick a coastal region or ocean and list countries which are likely to contribute to excess nutrients and algal blooms in that particular coast or ocean?

Q 7: Now look at Figure 4.3. We will be focusing on the North Sea, which is the part of the Atlantic Ocean between England and Norway. We will also be looking at the North Atlantic west of Ireland. What do you observe in comparing the images for February 12, 13, and 14? You can also go back to the Giovanni session and use the controls to slow down the loop or view each image individually.

Q 8: Look at Figure 4.4. This figure shows the average NO_2 tropospheric column over the area you selected over the North Sea. Which days had the highest NO_2 pollution levels?

Q 9: Now compare the individual Giovanni NO_2 maps for each day in February and compare them to the time series (Figure 4.4). Is there a correspondence between the two? What is the source of the variability in the OMI tropospheric NO_2 over the North Sea in February 2008?

4.4 Answers

A 1: The Netherlands in northern Europe have some of the highest NO_2 concentrations. England has very high concentrations as well. These are the countries in Europe with the highest concentrations of industrial activity.

A 2: The July levels are generally lower. There is greater photochemical destruction on NO_2 in the summer due to higher ozone concentrations. Heating sources in the winter that depend on fossil fuel combustion, such as coal, are used in the winter but not in the summer. Coal is a fossil fuel and a large source of NO_2

A 3: We would expect greater atmospheric NO_2 deposition in the winter. This would be true for all the oceans surrounding Europe where the atmospheric deposition is dominated by the sources (countries) shown in Figures 4.1a and b, and where there is little contribution from sources further away that are not shown in the map.

A 4: Spanish cities are more polluted than rural areas because they have more cars and industrial activities. Cars and other equipment that burn gasoline or diesel lead to NO_2 emissions. Industrial activities also use up a lot of energy that leads to NO_2 emissions.

A 5: The land areas are generally more polluted than the oceans. However, some of the coastal areas can be just as polluted as the land. This is because of their close proximity to atmospheric pollution sources. For example, there are values of NO_2 along the Southern Coast of France and along the coast of Italy that approach 6 to 7 x 10^{15} molecules/cm^2. Some of the oceans (Figure 4.1b) have values of NO_2 that can be quite large. This is because under certain atmospheric conditions, atmospheric NO_2 can also travel long distances over oceans. The Baltic Sea north of Poland has high pollution levels in January 2008. The Atlantic Ocean also experienced levels of

NO_2 that were comparable to land, particularly in the North Sea. The oceans where we would expect the worst problems with algal blooms would be those affected by large terrestrial or atmospheric sources of nutrients, including NO_2 from both. Phosphorus and sediments, when in excess, also contribute to water pollution and impacts such as algal blooms. Based on these maps, we would expect the Baltic Ocean and the North Sea in particular to receive a strong influence from atmospheric sources, and therefore these bodies of water would be more vulnerable to water pollution. Some portions of the Mediterranean Ocean such as coastal areas of Northern Italy would also be more vulnerable to water pollution due to atmospheric NO_2 deposition.

A 6: Over the Baltic, we would expect several contributing sources. All land areas that surround the Baltic Sea would contribute terrestrial sources of nutrients, including NO_2 from the rivers that feed into the Baltic Sea. Atmospheric sources of nutrients would be dominated by the surrounding countries with the highest levels or OMI tropospheric NO_2, primarily Germany, Poland, and Finland.

A 7: If you look at these figures in sequence you can see a plume of NO_2 over the North Sea on February 12th. On February 13th the plume moved west over the United Kingdom and Ireland, and by February 14th it has moved primarily offshore west of Ireland. The pollution over the North Sea on February 12th likely originated over northern Europe (the Netherlands, Belgium).

A 8: The highest NO_2 levels are on February 12th, 2008. However, there are other days later in the month, when the NO_2 tropospheric column increased again.

A 9: Go back and forth between the time series (Figure 4.4) and the maps for February 2008. There should be a correspondence between the two. If the map shows that the areas you selected had large NO_2 values, that should also be reflected as a peak in the time series. This variability is due to shifting meteorological patterns which cause varying degrees of transport of atmospheric NO_2 from land to the North Atlantic Ocean. You can select different regions (oceans) to create animation plots and time series and study the variability of atmospheric NO_2 and expected variability in water nutrient inputs.

4.5 References

Bucsela, EJ, Celarier EA, Wenig MO, Gleason JF, Veefkind JP, Boersma KF, and Brinksma E (2006) Algorithm for NO_2 vertical column retrieval from the Ozone Monitoring Instrument. IEEE Trans Geosci Rem Sens, 44, 1245-1258

Celarier EA, Brinksma EJ, Gleason JF, Veefkind JP, Cede A, Herman JR, Ionov D, Goutail F, Pommereau J-P, Lambert J-C et al. (2008) Validation of Ozone Monitoring Instrument nitrogen dioxide columns. J Geophysl Res 113: D15S15, doi:10.1029/ 2007JD008908

Duce, RA, LaRoche J, Altieri K, Arrigo KR, Baker AR, Capone DG, Cornell S, Dentener F, Galloway J, et al. , (2008) Impacts of Atmospheric Anthropogenic Nitrogen on the Open Ocean. Science 320 (5878) 893 [DOI: 10.1126/science.1150369]

Fanning KA (1989) Influence of atmospheric pollution on oceanic nutrient limitation. Nature 339: 460-463

Jickells, TD (1998) Nutrient biogeochemistry of the coastal zone. Science 281: 217-222 DOI: 10.1126/science.281.5374.217

Lamsal, LM, Martin RV, van Donkelaar A, Steinbacher M, Celarier EA, Bucsela E, Dunlea EJ Pinto JP (2008) Ground-level nitrogen dioxide concentrations inferred from the satellite-borne Ozone Monitoring Instrument. J Geophys Res 113: doi:10.1029/2007JD009235

Levy H II, Moxim WJ (1989) Simulated global distribution and deposition of reactive nitrogen emitted by fossil fuel combustion. Tellus 41B: 256-271

Prados, AI, Dickerson RR, Doddridge BG, Milne PA, Merrill JT, Moody JL (1999) Transport of ozone and pollutants from North America to the North Atlantic Ocean during the 1996 Atmosphere/Ocean Chemistry Experiment (AEROCE) Intensive. J Geophys Res 104: 26,219-26,233

Prados, AI, Leptoukh G, Johnson J, Rui H, Lynnes C, Chen A, Husar RB (2010) Access, visualization, and interoperability of air quality remote sensing data sets via the Giovanni online tool. IEEE J Selected Topics in Earth Observations and Remote Sensing. In press

Prospero JM, Barrett K, Church T, Dentener F, Duce RA, Galloway JN, Levy H II, Moody J Quinn P (1996) Atmospheric deposition of nutrients to the North Atlantic Basin. Biogeochem, 35 (1): 27-73

Pryor SC, and Sørensen LL (2002) Dry deposition of reactive nitrogen to marine environments: recent advances and remaining uncertainties, Marine Pollut Bull, 44 (12): 1336-1340, ISSN 0025-326X, DOI: 10.1016/S0025-326X(02)00234-5